

The MOSDEF Survey: The Metallicity Dependence of X-ray Binary Populations at $z \sim 2$ FRANCESCA M. FORNASINI,¹ MARISKA KRIEK,² RYAN L. SANDERS,³ IRENE SHIVAEI,^{4,5} FRANCESCA CIVANO,¹
NAVEEN A. REDDY,⁶ ALICE E. SHAPLEY,³ ALISON L. COIL,⁷ BAHRAM MOBASHER,⁶ BRIAN SIANA,⁶ JAMES AIRD,⁸
MOJEGAN AZADI,¹ WILLIAM R. FREEMAN,⁶ GENE C. K. LEUNG,⁷ SEDONA H. PRICE,⁹ TARA FETHEROLF,⁶ TOM ZICK,² AND
GUILLERMO BARRO¹⁰¹Center for Astrophysics | Harvard & Smithsonian, 60 Garden Street, Cambridge, MA 02138, USA²Astronomy Department, University of California, Berkeley, CA 94720, USA³Department of Physics & Astronomy, University of California, Los Angeles, 430 Portola Plaza, Los Angeles, CA 90095, USA⁴Department of Astronomy/Steward Observatory, 933 North Cherry Avenue, Room N204, Tucson, AZ, 85721-0065, USA⁵Hubble Fellow⁶Department of Physics & Astronomy, University of California, Riverside, 900 University Avenue, Riverside, CA 92521, USA⁷Center for Astrophysics and Space Sciences, University of California, San Diego, 9500 Gilman Drive, La Jolla, CA 92093-0424, USA⁸Department of Physics & Astronomy, University of Leicester, University Road, Leicester LE1 7RJ, UK⁹Max-Planck-Institut für extraterrestrische Physik, Postfach 1312, Garching, D-85741, Germany¹⁰Department of Physics, University of the Pacific, 3601 Pacific Avenue, Stockton, CA 95211, USA

(Accepted September 18, 2019)

Submitted to ApJ

ABSTRACT

Population synthesis models predict that high-mass X-ray binary (HMXB) populations produced in low metallicity environments should be more X-ray luminous, a trend supported by studies of nearby galaxies. This trend may be responsible for the observed increase of the X-ray luminosity (L_X) per star formation rate (SFR) with redshift due to the decrease of metallicity (Z) at fixed stellar mass as a function of redshift. To test this hypothesis, we use a sample of 79 $z \sim 2$ star-forming galaxies with oxygen abundance measurements from the MOSDEF survey, which obtained rest-frame optical spectra for ~ 1500 galaxies in the CANDELS fields at $1.37 < z < 3.80$. Using *Chandra* data from the AEGIS-X Deep, Deep Field North, and Deep Field South surveys, we stack the X-ray data at the galaxy locations in bins of redshift and Z because the galaxies are too faint to be individually detected. In agreement with previous studies, the average L_X/SFR of our $z \sim 2$ galaxy sample is enhanced by $\approx 0.4 - 0.8$ dex relative to local HMXB L_X -SFR scaling relations. Splitting our sample by Z , we find that L_X/SFR and Z are anti-correlated with 97% confidence. This observed Z dependence for HMXB-dominated galaxies is consistent both with the local L_X -SFR- Z relation and a subset of population synthesis models. Although the statistical significance of the observed trends is weak due to the low X-ray statistics, these results constitute the first direct evidence connecting the redshift evolution of L_X/SFR and the Z dependence of HMXBs.

Keywords: X-rays: binaries — X-rays: galaxies — galaxies: high redshift — galaxies: abundances

1. INTRODUCTION

Studies of nearby star-forming galaxies have established that the integrated X-ray luminosity (L_X) of high-mass X-ray binaries (HMXBs) in a galaxy is lin-

early correlated with its star formation rate (SFR; Ranalli et al. 2003; Grimm et al. 2003; Persic et al. 2004; Gilfanov et al. 2004; Lehmer et al. 2010; Mineo et al. 2012). This L_X -SFR correlation exists because of the young ages and short lifetimes of HMXBs, which consist of a black hole (BH) or neutron star (NS) accreting material from a high-mass ($M > 8M_\odot$) stellar companion. It is estimated that HMXBs form just $\sim 4\text{--}40$ Myr after a starburst and remain X-ray active only

for ~ 10 Myr (Iben et al. 1995; Bodaghee et al. 2012; Antoniou & Zezas 2016).

Several studies have found that the normalization of the L_X -SFR relation evolves with redshift (z), increasing by about 0.5 dex in L_X at fixed SFR between $z = 0 - 2$ (Basu-Zych et al. 2013a; Lehmer et al. 2016; Aird et al. 2017). On the contrary, Cowie et al. (2012) found no redshift evolution of L_X /SFR. However, Basu-Zych et al. (2013a) argued that this apparent lack of evolution results from the fact that Cowie et al. (2012) did not correct their SFR proxy, UV luminosity, for dust extinction, and Kaaret (2014) suggested that the anomalous Cowie et al. (2012) results may be attributed to their adoption of a spectral model that was not steep enough at hard X-ray energies. It has been suggested that the redshift evolution of L_X /SFR is driven by the metallicity (Z) dependence of HMXB populations and the fact that, on average, HMXBs at higher redshift have lower stellar metallicities.

Over the past decade, binary population synthesis studies have investigated the effects of metallicity on HMXB evolution. The winds of main-sequence high-mass stars are primarily driven by radiation pressure on atomic lines. Since high-mass stars primarily emit in the UV, and metals have far more UV atomic lines than H or He, the strength of their stellar winds is determined by their stellar metallicity. As a result, higher Z stars experience higher mass loss rates, losing more mass during the course of their lifetimes than lower Z stars. Therefore, the compact objects in low Z binaries are expected to be more massive than ones produced by stars of similar initial mass in higher Z binaries (Belczynski et al. 2004; Dray 2006; Fragos et al. 2013b). Another effect of the weaker winds of lower Z stars is that less angular momentum is lost from the binary, resulting in a larger fraction of HMXBs in which accretion occurs via Roche lobe overflow (Linden et al. 2010). Thus, lower Z HMXB populations are expected to contain larger fractions of Roche lobe overflow BH HMXBs, which are typically more luminous than wind-fed NS HMXBs. There is a general consensus that larger populations of luminous HMXBs exist in lower Z environments, although the strength of this trend varies between studies. Studies predict that L_X /SFR may increase by factor of 2 to 10 between Z_\odot and $0.1 Z_\odot$ (Linden et al. 2010; Fragos et al. 2013a).

In addition to informing models of binary stellar evolution, constraining the Z dependence of HMXB populations can yield insight into possible formation channels for the heavy BH binaries discovered by gravitational wave observatories (Abbott et al. 2016). Such BH binaries are thought to have evolved either from

HMXBs in a low Z environment (Belczynski et al. 2016) or through dynamical formation in dense stellar clusters (Rodríguez et al. 2016). Constraining the Z dependence of HMXBs is also critical for understanding their contribution to the X-ray heating of the intergalactic medium during the epoch of reionization when the Universe was extremely metal-poor (Mirabel et al. 2011; Madau & Fragos 2017), and informing models of the 21 cm power spectrum (e.g. Parsons et al. 2014). Furthermore, these constraints are important to accurately estimate the HMXB contamination to X-ray based searches for intermediate mass black holes (Mezcua 2017). Finally, properly calibrating for the Z dependence of HMXBs can improve the reliability of L_X as a SFR indicator (Brorby et al. 2016).

There is increasing observational evidence that a larger number of HMXBs, especially ultra-luminous X-ray sources (ULXs, $L_X \gtrsim 10^{39}$ erg s $^{-1}$), per unit SFR exist in nearby low Z galaxies (Mapelli et al. 2011; Kaaret et al. 2011; Prestwich et al. 2013; Basu-Zych et al. 2013b; Brorby et al. 2014; Douna et al. 2015). The enhanced number of bright HMXBs cannot be accounted for by stochasticity and suggests that at very low metallicities ($12 + \log(\text{O}/\text{H}) < 8.0$), the production rate of HMXBs is approximately 10 times higher than in solar metallicity ($12 + \log(\text{O}/\text{H}) = 8.69$) galaxies (Brorby et al. 2014; Douna et al. 2015). Using a compilation of measurements for 49 galaxies from the literature spanning $7.0 < 12 + \log(\text{O}/\text{H}) < 9.0$, Brorby et al. (2016) (hereafter B16) parametrize the L_X -SFR- Z correlation as:

$$\log \left(\frac{L_X / \text{SFR}}{\text{erg s}^{-1} / (\text{M}_\odot \text{ yr}^{-1})} \right) = b \times (12 + \log(\text{O}/\text{H}) - 8.69) + c \quad (1)$$

where the best-fitting parameters are $b = -0.59 \pm 0.13$ and $c = 39.49 \pm 0.09$. While this relation may be biased due to the mixture of sample selections for different galaxy samples taken from the literature, it provides the first observational benchmark of the L_X -SFR- Z relation at $z = 0$. However, it has not yet been shown that the Z dependence of HMXBs is the underlying cause of the observed redshift evolution of L_X /SFR.

We present the results of an X-ray stacking study of $z \sim 2$ star-forming galaxies drawn from the MOSFIRE Deep Evolution Field (MOSDEF) survey whose goal is to test this hypothesis observationally. The MOSDEF survey obtained rest-frame optical spectra for roughly 1500 galaxies at $1.4 < z < 3.8$ in CANDELS fields, which have been observed to deep limits with the *Chandra X-ray Observatory*; the combination of a large sample of high-redshift galaxies with robust Z measurements and deep X-ray data is what makes the study of the connection between the redshift evolution and Z

dependence of HMXBs possible for the first time. In §2, we describe the MOSDEF survey and the measurement of galaxy properties. §3 describes the *Chandra* X-ray data and catalogs used in this study. Sample selection and our X-ray stacking analysis are detailed in §4 and §5, respectively. In §6, we discuss our measurement of the Z dependence of L_X/SFR at $z \sim 2$ and compare it to the local $L_X\text{-SFR-}Z$ relation and theoretical models. Our conclusions are presented in §7. Throughout this work, we assume a cosmology with $\Omega_m = 0.3$, $\Omega_\Lambda = 0.7$, and $h = 0.7$ and adopt the solar abundances from Asplund et al. (2009) ($Z_\odot = 0.0142$, $12+\log(\text{O}/\text{H})_\odot = 8.69$).

2. THE MOSDEF SURVEY

Our $z \sim 2$ galaxy sample is selected from the MOSDEF survey (Kriek et al. 2015). This survey obtained moderate-resolution ($R = 3000\text{--}3650$) rest-frame optical spectra for ~ 1500 H -band selected galaxies using the MOSFIRE multi-object near-IR spectrograph (McLean et al. 2012) on the 10-meter Keck I telescope. MOSDEF targets are located in the CANDELS fields, where extensive multi-wavelength coverage is available (Grogin et al. 2011; Koekemoer et al. 2011). Possible MOSDEF target objects were selected from the 3D-HST photometric and spectroscopic catalogs (Skelton et al. 2014; Momcheva et al. 2016) to magnitude limits of $H = 24.0$, $H = 24.5$, and $H = 25.0$ for the low ($1.37 \leq z \leq 1.70$), middle ($2.09 \leq z \leq 2.61$), and high ($2.95 \leq z \leq 3.80$) redshift intervals, respectively. These magnitude limits roughly correspond to a lower mass limit of $\sim 10^9 M_\odot$.

The three redshift intervals were chosen to maximize coverage of strong rest-frame optical emission lines such that they fall within atmospheric transmission windows. Hereafter we will refer to these redshift intervals as $z \sim 1.5$, $z \sim 2.3$, and $z \sim 3.4$, respectively, and collectively refer to the galaxies in the two lowest redshift intervals as the $z \sim 2$ sample.

2.1. MOSDEF Data Reduction

The MOSFIRE spectra were reduced using a custom automated pipeline which performs flat-fielding, subtracts sky background, cleans cosmic rays, rectifies the frames, combines all individual exposures for a given source, and calibrates the flux (see Kriek et al. 2015 for details). Slit-loss corrections were determined by modeling the HST H -band light distribution of galaxies and calculating the amount of light passing through the slit, as detailed in Kriek et al. (2015) and Reddy et al. (2015). One-dimensional science and error spectra were optimally extracted based on the algorithm of Horne

(1986) (see the Appendix in Freeman et al. 2019 for details).

2.2. Emission lines fluxes and spectroscopic redshifts

Emission-line fluxes were measured by fitting Gaussian line profiles on top of a linear continuum to the one-dimensional spectra (Kriek et al. 2015; Reddy et al. 2015). The $H\alpha$ and $H\beta$ emission line fluxes were corrected for Balmer absorption using best-fit SED models, as described in Reddy et al. (2018). Flux uncertainties were estimated by performing 1,000 Monte Carlo realizations of the spectrum of each object perturbed by its error spectrum and refitting the line profiles; the average line fluxes and dispersions were measured from the resulting line flux distributions. Spectroscopic redshifts were measured using the centroids of the highest signal-to-noise ratio (S/N) emission lines, typically $H\alpha$ or [OIII] $\lambda 5007$. In total, the MOSDEF survey obtained spectroscopic redshifts for roughly 1300 objects, including galaxies that were specifically targeted and those that were serendipitously observed.

2.3. SED-derived M_* and SFR

Stellar masses were estimated by modeling the available photometric data (Skelton et al. 2014) for each galaxy with the spectral energy distribution (SED) fitting program FAST (Kriek et al. 2009), adopting the MOSDEF-measured spectroscopic redshift for each galaxy. The photometric data span rest-frame UV to near-IR wavelengths for $z \sim 2$ galaxies. We used the stellar population synthesis models of Conroy et al. (2009), assumed a Chabrier (2003) IMF, adopted the Calzetti et al. (2000) dust attenuation curve, and parametrized star-formation histories using delayed exponentially declining models of the form $\text{SFR}(t) \propto te^{-t/\tau}$, where t is the time since the onset of star formation and τ is the characteristic star formation timescale. For each galaxy, the best-fitting model was found through χ^2 minimization, and confidence intervals for all free parameters were calculated from the distributions of 500 Monte Carlo simulations which perturbed the input photometric data points and repeated the SED fitting procedure.

Since our goal is to study the relationship between L_X/SFR and Z , we explored the effect that SED-fitting assumptions can have on the derived SFR, particularly those assumptions that are Z -dependent (see §6.4). Therefore, we also used the results of SED fits from Reddy et al. (2018), which use the Bruzual & Charlot (2003) (hereafter BC03) stellar population models and vary the assumed dust attenuation curve (Calzetti et al. 2000 or SMC from Gordon et al. 2003) and the stellar

metallicity ($Z = 0.02$ or $Z = 0.004$). These SED fits assume constant SF histories, which have been shown to be appropriate for typical (L^*) galaxies at $z \gtrsim 1.5$ by previous studies (Reddy et al. 2012). Prior to SED-fitting, the photometry was corrected for the contribution from the strongest emission lines in the MOSFIRE spectra, including [O II], H β , [O III], and H α .

2.4. H α SFR

SFRs were also derived from dust-corrected H α luminosities. H α SFRs are sensitive to SF on shorter timescales and subject to partly different systematics than SED-derived SFRs. H α luminosities were corrected for dust attenuation using the absorption-corrected Balmer decrement (H α /H β) as described in Reddy et al. (2015) and Shivaie et al. (2015). These corrections assume the Cardelli et al. (1989) extinction curve, which Reddy et al. (in prep) find is consistent with the nebular reddening curve of MOSDEF $z \sim 2$ galaxies. The dust-corrected H α luminosities were converted into SFRs using the calibration of Hao et al. (2011) assuming a Chabrier (2003) IMF (conversion factor of $4.634 \times 10^{-42} M_{\odot} \text{ yr}^{-1} \text{ erg}^{-1} \text{ s}$). H α -derived SFRs are only calculated for galaxies in which both H α and H β are detected with $S/N \geq 3$.

Since this conversion factor depends on Z , Reddy et al. (2018) derive an alternative conversion factor that is more appropriate for the MOSDEF sample based on the BC03 $Z = 0.004$ ($0.28 Z_{\odot}$) model. This conversion factor is $3.236 \times 10^{-42} M_{\odot} \text{ yr}^{-1} \text{ erg}^{-1} \text{ s}$.

For our default SFR measurements, we adopt H α SFRs with a Z -dependent correction, wherein for galaxies with $12 + \log(\text{O}/\text{H}) > 8.3$, we apply the H α luminosity conversion factor appropriate for $Z = 0.02$ from Hao et al. (2011), and for galaxies with lower O/H, we adopt the conversion factor for $Z = 0.004$ from Reddy et al. (2018). Although we think these SFR measurements are the most robust, nonetheless in §6.4, we discuss the impact that our choice of SFR indicator has on our results.

While the SED-derived SFRs may not fully account for dust-obscured star formation because they are based on fitting rest-frame UV to near-IR data, the H α SFRs are found to be in good agreement with UV+IR SFRs. Shivaie et al. (2016) compared the H α SFRs of 17 MOSDEF galaxies detected by *Spitzer* MIPS and *Herschel* with SED-derived SFRs based on the UV to far-IR bands, and found strong agreement with 0.17 dex of scatter but no systematic biases.

2.5. Metallicity

The gas-phase metallicity of a galaxy is derived from the fluxes of emission lines originating from gas in

HII regions found near sites of recent star formation. Thus, the gas-phase oxygen abundance (O/H) is often used as a proxy for the stellar metallicity of the young stellar population of a galaxy, including its HMXBs. In order to facilitate the comparison of our results to the local L_X -SFR- Z relation, we adopt the same O/H indicator as Brorby et al. (2016), namely O3N2 ($\log([(\text{OIII})\lambda 5007/\text{H}\beta)/([\text{NII}]\lambda 6584/\text{H}\alpha))$). We use the calibration of Pettini & Pagel (2004), which is based on a sample of HII regions most of which have direct electron temperature measurements. This calibration is:

$$12 + \log(\text{O}/\text{H}) = 8.73 - 0.32 \times \text{O3N2} \quad (2)$$

We require that the four emission lines used for the O3N2 indicator are not significantly affected by nearby skylines or too close to the edge of the spectrum to measure the line flux reliably. If one or more of the emission lines required to calculate the O3N2 flux ratio was not detected with $S/N \geq 3$, then a 3σ upper limit on the line flux was computed and used to calculate an upper or lower limit on O/H.

Even though we are using the same O/H indicator as Brorby et al. (2016), it is possible that the O3N2 indicator evolves with redshift (Shapley et al. 2015; Sanders et al. 2016a) and that chemical abundances in galaxies at $z \sim 2$ differ from the solar pattern (Steidel et al. 2016; Sanders et al. 2019), affecting the relationship between gas-phase O/H and stellar metallicity. We discuss the systematic effects on our results due to these effects in §6.5.

2.6. AGN Identification

In order to study the X-ray binary (XRB) emission from MOSDEF galaxies, it is important to remove all known active galactic nuclei (AGN) from our sample. We identify AGN using diagnostics in multiple wavelength bands as detailed in Coil et al. (2015), Azadi et al. (2017), and Leung et al. (2017). The AGN identification criteria are summarized below and the possible impact of AGN contamination is discussed in §6.5.

2.6.1. X-ray AGN

All MOSDEF galaxies with *Chandra* counterparts were classified as X-ray AGN. Coil et al. (2015) matched *Chandra* sources detected by *wavdetect* with a false probability threshold $< 4 \times 10^{-6}$ in at least one of four energy bands (0.5–7, 0.5–2, 2–7, and 4–7 keV) to likely multi-wavelength counterparts using the likelihood ratio method described in Nandra et al. (2015); then the closest matches within $1''$ to these counterparts were found in the 3D-HST catalogs used for MOSDEF target selection. The X-ray detected MOSDEF galaxies at

$z > 1.3$ have high rest-frame 2–10 keV luminosities of $L_X > 10^{41.5}$ erg s $^{-1}$ indicative of AGN emission.¹

2.6.2. IR AGN

Since X-ray photons are absorbed at very high column densities ($N_H \gtrsim 10^{24}$ cm $^{-2}$), X-ray surveys can miss the most heavily obscured AGN. In these obscured sources, the high-energy AGN emission is processed by dust and re-radiated at mid-infrared (MIR) wavelengths. This phenomenon makes it possible to identify these obscured AGN based on their MIR colors. We select IR AGN using data from the Infrared Array Camera (IRAC; Fazio et al. 2004) on *Spitzer* reported in the 3D-HST catalogs (Skelton et al. 2014) and the IRAC color selection criteria defined by Donley et al. (2012).

2.6.3. Optical AGN

Optical diagnostics such as the “BPT diagram” (Baldwin et al. 1981; Veilleux & Osterbrock 1987) can be used to identify AGN via their enhanced ratios of nebular emission lines [OIII] λ 5008/H β and [NII] λ 6584/H α . However, since these diagnostics are based on the narrow components of emission lines, more detailed fitting of the H α , H β , [OIII], and [NII] emission lines is required to properly decompose the broad and narrow line components. As described in more detail in Azadi et al. (2017) and Leung et al. (2017), the emission lines were fit with up to three Gaussian components: a narrow, a broad, and a blueshifted component representing outflows. The broad and outflow components were only accepted if they resulted in an improved fit at $> 99\%$ confidence. Galaxies with significant broad lines were identified as optical AGN.

Using only the narrow line components, we placed galaxies on the BPT diagram. For this study, we flagged as an optical AGN any galaxy with $\log([\text{NII}]/\text{H}\alpha) > -0.3$ and any galaxy falling above the Kauffmann et al. (2003) line in the BPT diagram. Not all galaxies above the Kauffmann et al. (2003) line are expected to be AGN, especially at $z \gtrsim 2$ where galaxies are found to be offset to higher [NII]/H α values at fixed [OIII]/H β (Masters et al. 2014; Shapley et al. 2015; Sanders et al. 2016a; Strom et al. 2017). However, we choose to be conservative in our sample selection since even low-luminosity AGN emission may contaminate our measurements of X-ray luminosity, SFR, and O/H.

3. CHANDRA EXTRAGALACTIC SURVEYS

The *Chandra X-ray Observatory* has performed several deep extragalactic surveys. For this study, we use

the *Chandra* ACIS imaging in the *Chandra* AEGIS-X Deep, Deep Field North (CDF-N), and Deep Field South (CDF-S) fields. These fields have the deepest X-ray exposures, permitting the most complete identification and removal of X-ray AGN. The exposure depths reached in these fields is 7 Ms in CDF-S, 2 Ms in CDF-N, and 800 ks in AEGIS-XD (Alexander et al. 2003; Nandra et al. 2015; Luo et al. 2017). The corresponding flux limits (over $> 50\%$ of the survey area) in the 0.5–2 keV band reached by these surveys are 5×10^{-17} , 1.2×10^{-16} , and 2×10^{-16} erg cm $^{-2}$ s $^{-1}$, respectively, which correspond to 2–10 keV rest-frame X-ray luminosities of 1.2×10^{42} , 3.5×10^{42} , 5.8×10^{42} erg s $^{-1}$ at $z \sim 2$ assuming a power-law spectrum with a photon index of $\Gamma = 2.0$.

3.1. Chandra data processing

The *Chandra* data from the AEGIS-XD and CDF-N fields were processed as described in Laird et al. (2009), Rangel et al. (2013), Nandra et al. (2015), and Aird et al. (2015), and we made use of the publicly available *Chandra* mosaic images and exposure maps of the CDF-S field produced as described in Luo et al. (2017). The data were processed using the CIAO analysis software v4.1.2 and v4.8 for the former and latter data sets respectively. The data processing procedures applied to all three datasets are very similar and are briefly summarized below with full details provided in Nandra et al. (2015) and Luo et al. (2017).

Each observation was cleaned and calibrated using standard CIAO algorithms. For each observation, the *Chandra* wavelet source detection algorithm `wavdetect` was run on the 0.5–7 keV band image with a detection threshold of 10^{-6} . The astrometry of individual observations was improved by using the CIAO tool `reproject_aspect` to minimize the offsets between `wavdetect` sources and counterparts in the Canada-France-Hawaii Telescope Legacy survey (CFHTLS) *i*-band catalog (Gwyn 2012) for AEGIS-XD, the *r*-band Hawaii HDFN catalog Capak et al. (2004) for CDF-N, and the Taiwan ECDFS Near-Infrared Survey (TENIS) Ks-band catalog (Hsieh et al. 2012) for CDF-S.

3.2. Chandra data products and catalogs

For each individual observation, event files, images, exposure maps, and PSF maps of the 90% encircled energy fraction (EEF) as calculated by the MARX simulator were created for the 0.5–7, 0.5–2, and 2–7 keV bands. The exposure maps provide the exposure multiplied by the effective collecting area at each pixel location; they are weighted for a power-law spectrum with $\Gamma = 1.4$, the photon index of the cosmic X-ray background (Gruber et al. 1999; Ajello et al. 2008;

¹ In fact, all but one of the X-ray detected MOSDEF galaxies at $z > 1.3$ have $L_X > 10^{42.5}$ erg s $^{-1}$.

Cappelluti et al. 2017).² The event files, images, exposure maps, and PSF maps for each field were merged together into the mosaics used in our X-ray stacking analysis (see §5).

We compared the astrometric frame of these final mosaics to the astrometry of the 3D-HST catalogs from which the MOSDEF galaxy positions are determined. For each X-ray detected counterpart of a MOSDEF galaxy with > 40 net counts in the $0.5 - 7$ keV band, we calculated the (x, y) positional offset between its coordinates from the 3D-HST catalog and its centroid coordinates measured using the `gcntrd` IDL program. In the AEGIS, GOODS-S, and GOODS-N fields, there are 9, 6, and 23 such counterparts to MOSDEF galaxies. For each field, we then determined the average x and y offset, and found them to be < 1 pixel in all cases. We apply these positional shifts to ensure the best match between the *Chandra* mosaics and the astrometric reference frame of MOSDEF galaxies. However, we note that because the X-ray aperture regions used in our stacking analysis are at least 4 pixels in diameter, these small positional shifts do not significantly impact the derived X-ray properties of our stacks.

In order to study the XRB emission of non-AGN MOSDEF galaxies, it is important to reduce not only contamination from MOSDEF AGN but also the contribution from nearby detected X-ray sources that are not associated with MOSDEF galaxies. X-ray source catalogs for the CDF-S, CDF-N, and AEGIS-XD surveys are provided by Luo et al. (2017), Alexander et al. (2003), and Nandra et al. (2015), respectively. We use these catalogs to remove the contribution of detected *Chandra* sources to our X-ray stacks as detailed in §5.

4. GALAXY SAMPLE SELECTION

Since our goal is to study HMXB emission as a function of Z and SFR, we apply several selection criteria to select galaxies with reliably measured properties and to minimize contamination from other X-ray sources.

Therefore, we excluded from our sample any MOSDEF galaxy that is identified as an AGN using the X-ray, IR, or optical criteria described in §2.6. The other sources that can contribute significantly to a galaxy's hard X-ray emission are low-mass X-ray binaries (LMXBs), whose X-ray emission is correlated with the stellar mass (M_*) of a galaxy (Gilfanov 2004; Colbert et al. 2004). Thus, the X-ray contribution of HMXBs relative to LMXBs is maximized in galaxies with high specific SFR ($s\text{SFR} = \text{SFR}/M_*$). Studies of

local galaxies find that galaxies with $s\text{SFR} > 10^{-10} \text{ yr}^{-1}$ are HMXB-dominated (Lehmer et al. 2010), which is true of all galaxies in our MOSDEF sample. However, the $s\text{SFR}$ value at which galaxies transition from being LMXB-dominated to HMXB-dominated may increase with redshift (Lehmer et al. 2016). Considering that this value for $z \sim 2$ galaxies remains poorly constrained, we study how restricting our sample to different $s\text{SFR}$ ranges affects our results. Our MOSDEF galaxies span a $s\text{SFR}$ range of $10^{-9.6} - 10^{-8.1} \text{ yr}^{-1}$ with a median $s\text{SFR}$ of $10^{-8.8} \text{ yr}^{-1}$.

We required that galaxies have an O/H measurement or upper/lower limit based on the O3N2 indicator in order to facilitate comparison to local studies of the Z dependence of HMXBs (Douna et al. 2015; Brorby et al. 2016). In addition, we restricted our sample to galaxies with both $\text{H}\alpha$ and SED-derived SFRs. We further limited our galaxy sample to $M_* \geq 10^{9.5} M_\odot$, because Shivaie et al. (2015) demonstrated that MOSDEF samples may be incomplete at lower M_* due to a bias against young objects with small Balmer and 4000 Å breaks. Furthermore, the MOSDEF survey may not be complete in $\text{H}\alpha$ SFRs for $M_* < 10^{9.5} M_\odot$, because we would expect that such low-mass galaxies scattering below the M_* -SFR relation (Sanders et al. 2018) would fall below the 3σ $\text{H}\beta$ detection limit.

As mentioned in §3, even though the MOSDEF survey covers all the CANDELS fields, we only included galaxies from the GOODS-S (Giavalisco et al. 2004), GOODS-N (Giavalisco et al. 2004), and AEGIS (Davis et al. 2007) fields; the *Chandra* survey of the COSMOS field (Scoville et al. 2007) is much shallower (Civano et al. 2016), and in the UKIDSS-UDS field (Lawrence et al. 2007) only 34 galaxies were observed as a part of MOSDEF, just a few of which meet our selection criteria. Furthermore, only galaxies in the $z \sim 1.5$ and $z \sim 2.3$ redshift intervals are used. The galaxy sample at $z \sim 3.4$ is too small to produce significant X-ray stacked detections and, at these high redshifts, the $\text{H}\alpha$ and [NII] emission lines move out of the near-infrared band, requiring different diagnostics to screen optical AGN and to measure Z and SFR.

Finally, we imposed two additional restrictions in order to optimize the *Chandra* stacking procedure described in §5. These criteria are based on the size of the PSF at the galaxy position and proximity to other sources.

Only 79 MOSDEF galaxies meet all our selection criteria. Figure 1 displays the $\text{H}\alpha$ SFR versus stellar mass for the galaxies in our sample in points colored by the oxygen abundance and outlined in blue or black for $z \sim 1.5$ and $z \sim 2.3$, respectively. The gray dots in this fig-

² Adopting a different value of Γ in the range from 1.0 to 2.0 would change the exposure map values by $< 10\%$.

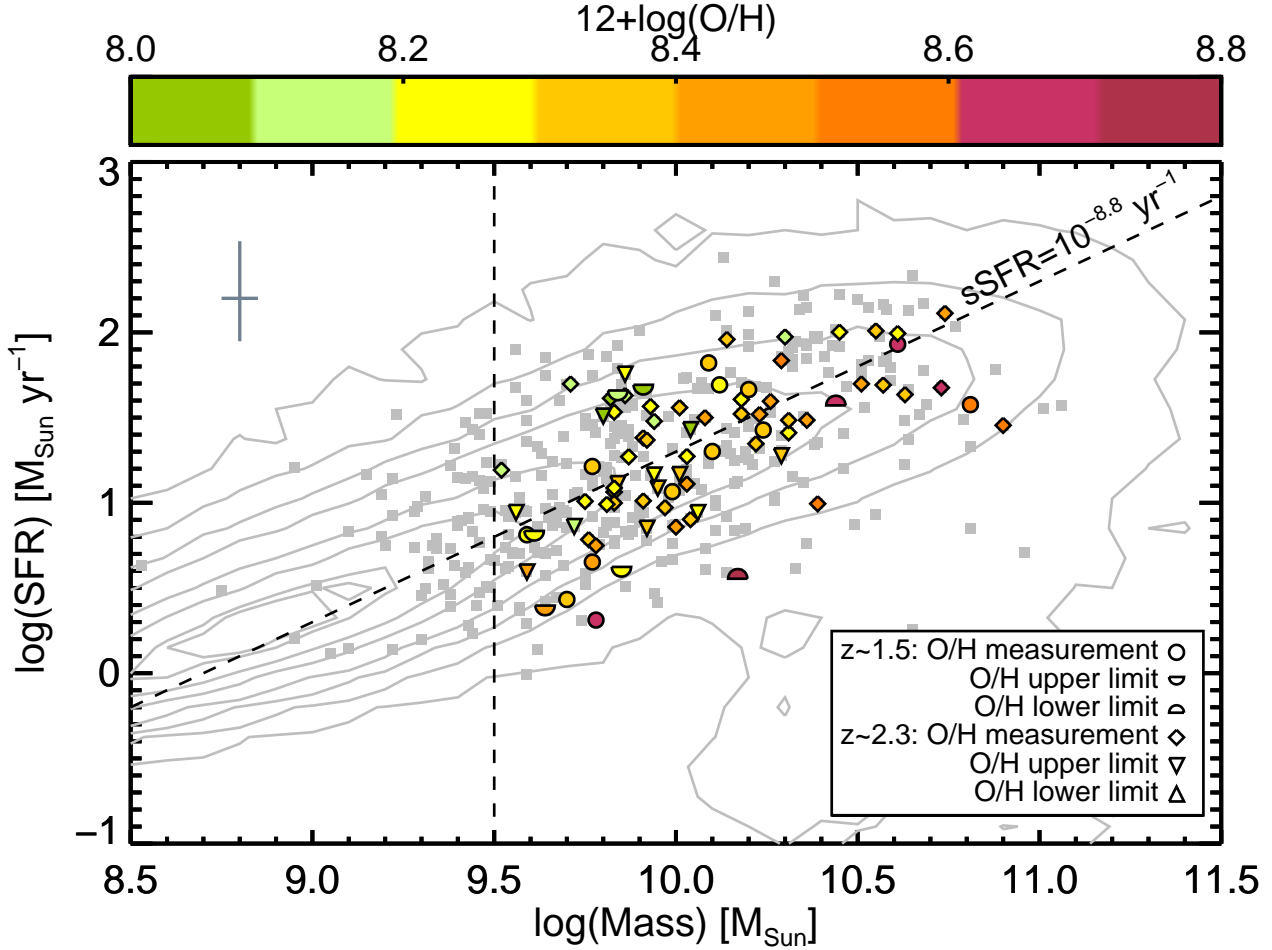


Figure 1. $H\alpha$ SFRs of MOSDEF galaxies versus M_* derived from SED fitting. The gray squares show all MOSDEF galaxies with $H\alpha$ -derived SFRs and no AGN signatures. The 79 galaxies used in our analysis are shown by symbols colored according to Z . The circle, lower half circle, and upper half circle symbols represent galaxies at $1.37 \leq z \leq 1.70$ with O/H measurements, upper limits, or lower limits, respectively. The diamond, downward triangle, and upward triangle symbols represent galaxies at $2.09 \leq z \leq 2.61$ with O/H measurements, upper limits, or lower limits, respectively. The median 1σ uncertainty in SFR and M_* measurements is shown in the upper left corner. The MOSDEF galaxies are well-distributed along the main sequence of star-forming galaxies shown by the gray contours, which are based on the distribution of galaxies with $1.37 \leq z \leq 2.61$ from the COSMOS field (Laigle et al. 2016). The vertical dashed line represents our M_* selection threshold, while the diagonal dashed line represents our division of the sample into high and low sSFR galaxies ($sSFR = 10^{-8.8} \text{ yr}^{-1}$).

ure represent all MOSDEF galaxies with $1.4 < z < 2.7$ and $H\alpha$ -derived SFRs, and the gray contours are based on the SED-derived SFRs and M_* from a much larger sample of $\sim 160,000$ galaxies in the COSMOS field with photometric redshifts in the same z range (Laigle et al. 2016). As can be seen, even though our sample is small, it is representative of star-forming galaxies at $z \sim 2$. Sanders et al. (2018) found evidence that a M_* -SFR- Z relation exists in MOSDEF galaxies at $z \sim 2.3$, a hint of which can be observed in Figure 1 as galaxies with higher SFR at fixed M_* have lower Z . As shown in Figure 2, 20 galaxies are at $z \sim 1.5$ and 59 are at $z \sim 2.3$. The Z distribution of our sample is shown in Figure 3, with $12+\log(O/H)$ measurements, 3σ upper, and 3σ

lower limits indicated in different colors. The Z distribution is strongly peaked at $12+\log(O/H) = 8.3-8.4$.

5. X-RAY STACKING ANALYSIS

The typical X-ray luminosities of normal (non-AGN) star-forming galaxies are $L_X < 10^{42} \text{ erg s}^{-1}$ in the rest-frame 2–10 keV band.³ Since these luminosities fall below the sensitivity limits of the *Chandra* extragalactic surveys at $z \sim 2$, studying the X-ray emission of these galaxies requires stacking the X-ray data. We de-

³ Low luminosity AGN and/or obscured AGN can also exhibit $L_X < 10^{42} \text{ erg s}^{-1}$. We discuss possible contamination from such AGN in §6.5.

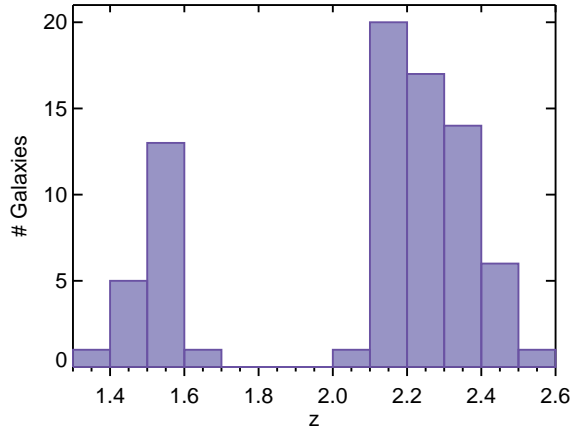


Figure 2. The redshift distribution of the 79 galaxies used for our study. The distribution is bimodal because MOSDEF targets were selected in specific redshift windows ($1.37 \leq z \leq 1.70$ and $2.09 \leq z \leq 2.61$) for which rest-frame optical strong emission lines fall within atmospheric transmission windows. There are more galaxies with $z \sim 2.3$ than $z \sim 1.5$ as a result of the MOSDEF survey’s targeting strategy (Kriek et al. 2015).

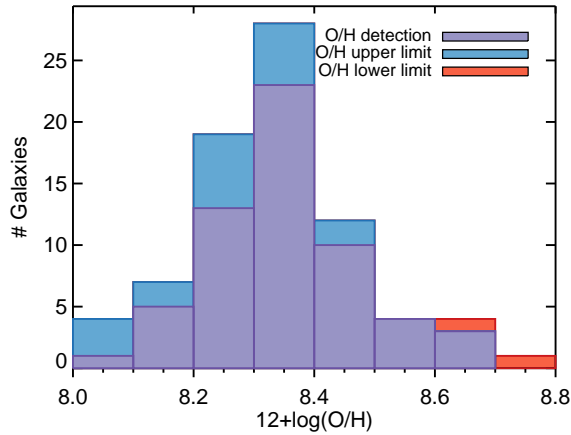


Figure 3. The distribution of Z of the galaxies in our sample, as traced by nebular O/H based on the O3N2 indicator. O/H measurements (calculated when all relevant emission lines are significantly detected) are shown in purple, while O/H upper and lower limits are shown in blue and red, respectively.

veloped an X-ray stacking technique that is similar to that used by other studies (e.g. Basu-Zych et al. 2013a; Rangel et al. 2013; Mezcua et al. 2016; Fornasini et al. 2018). In order to achieve the highest sensitivity, we performed the stacking primarily using the 0.5–2 keV band because *Chandra* has the highest effective area and best angular resolution at soft X-ray energies. However, we

also stacked the data in the 2–7 keV band in order to measure the hardness ratios for our stacks.

5.1. X-ray photometry for individual sources

For each of the galaxies in our sample, we defined source and background aperture regions. Each source aperture was defined as a circular region centered on the galaxy position from the 3D-HST catalog with a radius equal to the 90% ECF PSF radius (r_{90}). The median r_{90} of MOSDEF objects is $2.4''$, and their angular sizes are small enough that their galaxy-wide X-ray emission is consistent with a point source. Each background aperture was defined as an annulus with an inner radius equal to $10''$ and an outer radius equal to $30''$.

As mentioned in 4, we made some refinements to our galaxy sample based on X-ray criteria. In order to prevent contamination to our source or background count estimates from unassociated X-ray sources, we masked out from the images and exposure maps circular regions with a radius of $2r_{90}$ at the positions of any X-ray detected sources in the CDF-S, CDF-N, and AEGIS-XD source catalogs (Alexander et al. 2003; Luo et al. 2017; Nandra et al. 2015), regardless of what energy band the source was detected in. We removed from our sample any galaxy at a distance $< 2r_{90}$ of an X-ray detected source. We also excluded any galaxies at a distance $< r_{90}$ from another galaxy in the 3D-HST catalog with H_{AB} (F160W) magnitude < 24.0 , which is the magnitude limit approximately corresponding to $M_* = 10^{9.5} M_\odot$ at $z \sim 2.3$. These sources were excluded to avoid contamination from neighboring galaxies with X-ray emission below the sensitivity threshold of the *Chandra* surveys but potentially of comparable or greater luminosity as our MOSDEF galaxies. We also removed four galaxies located in an area of diffuse X-ray emission in the CDF-N field. Finally, to optimize the signal-to-noise ratio, we excluded galaxies located far off-axis in the *Chandra* observations as the *Chandra* PSF increases with off-axis angle; we find that the significance of our stacks is maximized by excluding sources with $r_{90} > 3.5''$.

We extracted the counts (C_{src} , C_{bkg}), effective exposure time (t_{src} , t_{bkg}), and apertures areas in units of pixels^2 (A_{src} , A_{bkg}) for both the source and background regions for each galaxy using the CIAO tool `dmextract`. The effective exposure accounts for variations across the field of view due to the telescope optics, CCD gaps, and bad pixels. The background region counts were extracted from the annular background regions, from which any X-ray detected sources as well as all MOSDEF galaxies were masked out. Our measurements of

the aperture areas account for any fraction of the area that was masked out.

For each source, we calculated the net background-subtracted counts and a conversion factor to translate the net counts into the rest-frame X-ray luminosity. The net source counts (C_{net}) are calculated as:

$$C_{\text{net}} = C_{\text{src}} - C_{\text{bkg}} \times \frac{t_{\text{src}} A_{\text{src}}}{t_{\text{bkg}} A_{\text{bkg}}} \quad (3)$$

Converting the net counts in the 0.5–2 keV band into rest-frame 2–10 keV luminosities requires assuming a spectral model to calculate the mean energy per photon (E_{avg}) and the k -correction (k_{corr}). We assume an unobscured power-law spectrum with $\Gamma = 2.0$ to facilitate comparison with the local L_X -SFR- Z relation measured by Brorby et al. (2016). In Section 6.5, we discuss the validity and uncertainty associated with this assumption. For each source, we calculate the conversion factor, ω , between net counts and X-ray luminosity, as given by:

$$L_X = C_{\text{net}} / \omega \quad (4)$$

$$\omega = (t_{\text{src}} \text{ECF}) / (4\pi D_L^2 E_{\text{avg}} k_{\text{corr}})$$

where D_L is the luminosity distance and $\text{ECF} = 0.9$ since our aperture regions are based on 90% PSF radius.

5.2. Stacked X-ray luminosities

For a given galaxy stack, we summed the net counts and the expected number of background counts from individual source apertures. The average X-ray luminosity ($\langle L_X \rangle$) of a stack of N galaxies is calculated as the total net counts divided by the sum of the conversion factors:

$$\langle L_X \rangle = \frac{1}{N} \sum_i^N \frac{C_{\text{net},i}}{\omega_i} \approx \frac{\sum_i^N C_{\text{net},i}}{\sum_i^N \omega_i} \quad (5)$$

This approximation is appropriate when the galaxies in a given stack have similar L_X . We expect the range of L_X for galaxies in a given Z bin to primarily be set by the range of SFR, and therefore to span at most 2 orders of magnitude. For such a range of L_X , we estimate that the approximation we use to measure $\langle L_X \rangle$ should be accurate to 0.1 dex. The conversion factor ω associated with each galaxy provides a relative weighting for how much each galaxy contributes to the measured X-ray emission. Since our goal is to study the relationship between L_X and different galaxy properties (i.e. SFR, Z , z , M_* , sSFR), for each galaxy stack we also calculate the weighted average of each galaxy property, applying the ω factors used to calculate the X-ray luminosity. We estimate that our measurement of $\langle L_X \rangle / (\text{SFR})$ should approximate $\langle L_X / \text{SFR} \rangle$ with an accuracy of 0.05 dex

based on the scatter of 0.3–0.4 dex observed in the local L_X -SFR- Z relation (Brorby et al. 2016).

We computed two sources of error on each stacked signal. The first is Poisson noise associated with the background, which we used to establish the significance of the signal in each stack. We calculated the Poisson probability that a random fluctuation of the estimated background counts could result in a number of counts within the source regions greater than or equal to the total stacked counts (source plus background).

Table 1 provides information about the properties of galaxies in our stacks, including the weighted average redshift, M_* , and SFR, as well as the median stacked O/H. The X-ray properties of our stacks, including the signal significance, net counts, and mean L_X , are presented in Table 2. We tested that our stacking procedure does not result in an unusual number of spurious detections by stacking the *Chandra* data at random sky positions rather than galaxy positions. We apply the same X-ray selection criteria to the random positions as our galaxy sample. We make 500 mock stacks for each of the 10 real stacks described in Table 1; each mock stack includes the same number of individual positions per *Chandra* survey field as its corresponding real stack. For each mock stack, we calculate the probability that the total stacked counts could be due to a random fluctuation of the estimated background. The resulting probability distributions of the mock stacks is consistent with expectations for random noise (e.g. 1% of mock stacks have a 1% probability of being due to random noise). Thus, the detection probabilities of our real stacks are reliable.

The statistical uncertainties associated with the measured X-ray luminosities are calculated using a bootstrapping method, which measures how the contribution of individual sources affects the average stacked signal. To determine the bootstrapping errors, we randomly resampled the galaxies in each stack 1000 times and repeated our stacking analysis. The number of galaxies in a given stack is conserved during the resampling, leading some values to be duplicated while others are eliminated in a particular iteration. From the resulting distribution of stacked X-ray luminosities, we measure 1σ confidence intervals for stacked signals exceeding our detection threshold.

As done in Lehmer et al. (2016), the uncertainties associated with the weighted average galaxy properties ($\langle Q_{\text{phys}} \rangle$) are also calculated by a bootstrapping technique. Each galaxy value is perturbed according to its error distribution and the weighted average is recalculated. The calculation of these perturbed average values ($\langle Q_{\text{phys},k}^{\text{pert}} \rangle$) is performed 1000 times and the 1σ uncer-

tainty on the weighted average is according to the following equation:

$$\sigma_{\langle Q_{\text{phys}} \rangle} = \frac{1}{N_{\text{boot}}} \left[\sum_{k=0}^{N_{\text{boot}}} (\langle Q_{\text{phys},k}^{\text{pert}} \rangle - \langle Q_{\text{phys}} \rangle)^2 \right]^{1/2} \quad (6)$$

The weighted average galaxy properties for each stack discussed in §6 are provided in Table 1, while the stacked X-ray properties are listed in Table 2.

5.3. Stacked Metallicity Measurements

To maximize our sample size and reduce biases in our galaxy sample, in our stacking analysis we include galaxies with upper or lower limits on their oxygen abundance based on the O3N2 indicator. For parts of our analysis we split our sample into different z bins. In the highest z bin, we include galaxies with $12+\log(\text{O}/\text{H})$ lower limits higher than the bin's lower bound, and in the lowest z bin, we include galaxies with $12+\log(\text{O}/\text{H})$ upper limits lower than the bin's upper bound. Overall, for the 79 galaxies in our full sample, we have 59 O/H measurements, 18 upper limits, and 2 lower limits.

Due to the inclusion of upper and lower limits on $12+\log(\text{O}/\text{H})$, we cannot simply average the O/H values of the galaxies in each stack. Instead, using the method of Sanders et al. (2015), we measure the stacked O/H by making composite spectra of the galaxies in each stack. Each galaxy spectrum was shifted to rest frame, converted from flux density to luminosity density, corrected for reddening assuming the Cardelli et al. (1989) attenuation curve, interpolated onto a common wavelength grid, and normalized by the $\text{H}\alpha$ luminosity. Normalized composite spectra were created by taking the X-ray weighted (ω) median value of the normalized spectra. Emission-line luminosities were measured from the composite spectra by fitting a flat continuum and Gaussian profiles to regions around emission features. Uncertainties were estimated using a Monte Carlo technique. Testing this method using only galaxies with detections of all lines of interest, this stacking method was found to robustly reproduce the X-ray weighted median line ratios of the galaxies in a stack.

6. RESULTS AND DISCUSSION

6.1. The redshift evolution of XRBs

We first investigate whether our galaxy sample supports the redshift evolution of L_X/SFR of XRBs found by previous studies (e.g. Lehmer et al. 2016; Aird et al. 2017). We use X-ray stacks of our full $z \sim 2$ sample as well as the subsample of galaxies with $\text{sSFR} > 10^{-8.8} \text{ yr}^{-1}$. These high sSFR stacks should be dominated by HMXBs, while the full sample stacks likely contain significant contributions from both LMXBs and

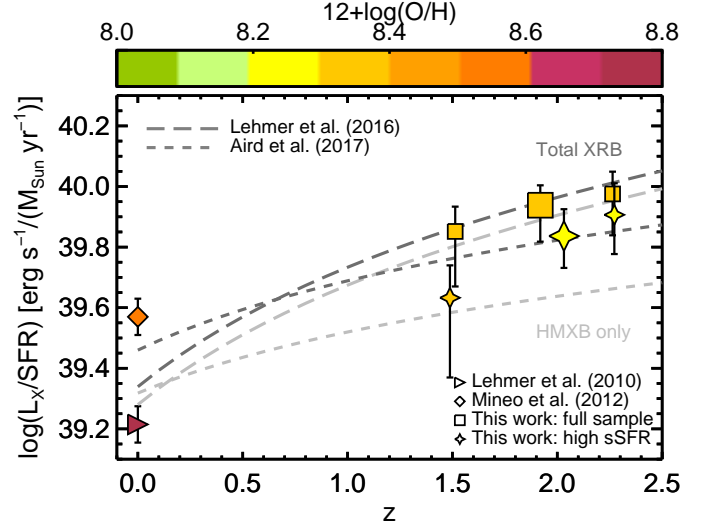


Figure 4. Stacked L_X/SFR values of our galaxy sample split into $z \sim 1.5$ and $z \sim 2.3$ redshift bins are shown by small squares/stars; squares represent stacks of the full galaxy sample, stars represent stacks of high sSFR ($\text{sSFR} > 10^{-8.8} \text{ yr}^{-1}$) galaxies that are HMXB-dominated, and colors represent the weighted median oxygen abundance of the stacks. The larger square (star) symbol represents the combined $z \sim 2$ stack of all (high sSFR) galaxies. The colored diamond and triangle represent local ($z = 0$) measurements of the L_X -SFR relation. The long and short dashed lines show the redshift evolution of L_X/SFR for the total XRB (dark gray) and HMXB-only (light gray) emission derived by Lehmer et al. (2016) and Aird et al. (2017); since the L16 total XRB evolution and the A17 HMXB-only evolution are parametrized as non-linear relations between L_X and SFR, these curves have been normalized for $\text{SFR} = 20 M_\odot \text{ yr}^{-1}$, the mean SFR of our $z \sim 2$ galaxy sample. Our stacks lie above the $z = 0$ measurements and are consistent with the redshift evolution measured by previous studies.

HMXBs, as discussed in more detail in §6.3. Since our galaxy sample is bimodally distributed in redshift due to atmospheric windows (see Figure 2), we also split the galaxy sample between these two redshift intervals: $1.3 < z < 1.7$ and $2.0 < z < 2.6$. Information for all the aforementioned stacks is provided in rows #1 – 3 and 10 – 12 of Tables 1 and 2. The full sample redshift stacks are represented by colored squares in Figure 4, while the high sSFR stacks are shown by colored stars.

In Figure 4, we also show L_X/SFR values measured by two studies (Lehmer et al. 2010; Mineo et al. 2012, hereafter L10 and M12, respectively) using samples of nearby galaxies at $z = 0$. The M12 value is converted from the 0.5 – 8 to 2 – 10 keV band assuming $\Gamma = 2.0$ and $N_{\text{H}} = 3 \times 10^{21} \text{ cm}^{-2}$, the average column density measured for their galaxy sample. Both the L10 and M12 values are converted to be consistent with a Chabrier IMF. The 0.3 dex difference between these lo-

Table 1. Average Galaxy Properties of Stacks

Stack ID	# Galaxies				$\langle z \rangle$	$\log \langle M_* \rangle$ (M_\odot)	12+log(O/H)	SFR Indicator	$\langle \text{SFR} \rangle$ ($M_\odot \text{ yr}^{-1}$)	$\log \langle \text{sSFR} \rangle$ (yr^{-1})
	All	AEGIS	CDF-N	CDF-S						
(a)	(b)	(c)	(d)	(e)	(f)	(g)	(h)	(i)	(j)	(k)
All sSFR										
1	79	53	22	3	1.92	$10.121^{+0.002}_{-0.001}$	8.31 ± 0.01	H α , corr	$22.9^{+0.7}_{-0.3}$	$-8.738^{+0.009}_{-0.004}$
All sSFR: redshift binning										
2	20	13	7	0	1.51	$10.053^{+0.002}_{-0.001}$	8.32 ± 0.02	H α , corr	$16.6^{+0.5}_{-0.2}$	$-8.856^{+0.010}_{-0.004}$
3	59	41	15	3	2.26	10.172 ± 0.001	8.31 ± 0.01	H α , corr	$28.3^{+0.9}_{-0.4}$	$-8.658^{+0.009}_{-0.004}$
All sSFR: metallicity binning										
4	30	19	8	3	2.05	$9.971^{+0.002}_{-0.001}$	$8.23^{+0.01}_{-0.02}$	H α , corr	$22.6^{+0.7}_{-0.3}$	$-8.606^{+0.006}_{-0.003}$
5	23	19	4	0	1.82	$10.110^{+0.002}_{-0.001}$	8.35 ± 0.01	H α , corr	$27.3^{+0.8}_{-0.3}$	$-8.711^{+0.013}_{-0.005}$
6	19	13	6	0	1.78	10.337 ± 0.002	8.52 ± 0.02	H α , corr	$25.4^{+0.9}_{-0.3}$	$-8.983^{+0.014}_{-0.005}$
Restricting sSFR: metallicity binning										
$-9.3 < \log(\text{sSFR})_{\text{H}\alpha, \text{corr}} < -8.4$										
7a	24	15	7	2	2.04	10.001 ± 0.001	$8.24^{+0.01}_{-0.02}$	H α , corr	$20.6^{+0.6}_{-0.2}$	$-8.705^{+0.005}_{-0.002}$
8a	21	17	4	0	1.83	10.110 ± 0.001	8.35 ± 0.01	H α , corr	$23.4^{+0.7}_{-0.3}$	$-8.791^{+0.013}_{-0.005}$
9a	15	11	4	0	1.86	$10.408^{+0.002}_{-0.001}$	$8.45^{+0.02}_{-0.03}$	H α , corr	$36.2^{+1.3}_{-0.5}$	$-8.849^{+0.014}_{-0.006}$
$-9.2 < \log(\text{sSFR})_{\text{H}\alpha} < -8.4$										
7b	18	9	7	1	2.01	10.019 ± 0.001	8.22 ± 0.02	H α	$26.0^{+0.7}_{-0.3}$	$-8.650^{+0.011}_{-0.004}$
8b	20	17	3	0	1.94	10.177 ± 0.001	8.38 ± 0.01	H α	$28.9^{+0.9}_{-0.4}$	$-8.720^{+0.014}_{-0.005}$
9b	14	10	4	0	1.89	$10.343^{+0.002}_{-0.001}$	$8.45^{+0.02}_{-0.03}$	H α	$36.0^{+1.3}_{-0.5}$	$-8.827^{+0.014}_{-0.006}$
$-9.05 < \log(\text{sSFR})_{\text{SED}} < -8.5$										
7c	22	13	8	1	2.05	9.980 ± 0.001	$8.25^{+0.01}_{-0.02}$	SED	$19.4^{+0.2}_{-0.1}$	$-8.663^{+0.005}_{-0.003}$
8c	22	18	4	0	1.81	$10.113^{+0.002}_{-0.001}$	$8.35^{+0.01}_{-0.01}$	SED	22.0 ± 0.2	$-8.801^{+0.005}_{-0.003}$
9c	15	10	5	0	1.75	$10.192^{+0.002}_{-0.001}$	8.50 ± 0.02	SED	$25.3^{+0.3}_{-0.2}$	$-8.851^{+0.005}_{-0.003}$
High sSFR: $\log(\text{sSFR}) > -8.8$										
10	37	26	6	3	2.03	$10.117^{+0.002}_{-0.001}$	$8.30^{+0.01}_{-0.02}$	H α , corr	$37.5^{+1.2}_{-0.5}$	$-8.508^{+0.009}_{-0.004}$
High sSFR: redshift binning										
11	8	7	1	0	1.49	$10.140^{+0.003}_{-0.001}$	$8.31^{+0.01}_{-0.03}$	H α , corr	$39.0^{+1.2}_{-0.5}$	$-8.510^{+0.011}_{-0.005}$
12	29	21	5	3	2.27	10.106 ± 0.001	$8.29^{+0.01}_{-0.02}$	H α , corr	$36.9^{+1.2}_{-0.5}$	$-8.508^{+0.008}_{-0.004}$
High sSFR: metallicity binning										
13	19	12	4	3	2.12	$10.012^{+0.002}_{-0.001}$	8.23 ± 0.02	H α , corr	$30.2^{+0.9}_{-0.4}$	$-8.493^{+0.006}_{-0.003}$
14	17	15	2	0	1.87	$10.264^{+0.002}_{-0.001}$	8.40 ± 0.01	H α , corr	$51.6^{+1.7}_{-0.7}$	$-8.530^{+0.014}_{-0.006}$

Notes:

(h) X-ray weighted, median oxygen abundance of the galaxy stack based on O3N2 indicator (Pettini & Pagel 2004).

(i) SED SFR listed assumes $Z = 0.02$, Calzetti extinction curve, and constant SF history. The H α indicator assumed $Z = 0.02$ and the Cardelli extinction curve. For the H α , corr indicator, the conversion factor for galaxies with $12 + \log(\text{O}/\text{H}) < 8.3$ assumes $Z = 0.004$ and the Cardelli extinction curve.

cal values is likely due to sample selection effects. In fact, it is possible that the average metallicity of the galaxies in the L10 and M12 differs significantly. Metallicity information is not available for all the galaxies in the L10 or M12 samples. Therefore, we estimate the mean O/H for the L10 sample using the $M_* - Z$ relation from Kewley & Ellison (2008) based on the O3N2 calibration by (Pettini & Pagel 2004), and by combining the O/H measurements for 19 of the M12 galaxies gathered by Douna et al. (2015) and estimates based on the $M_* - Z$ relation for the remaining 10 M12 galaxies. As shown by the colorbar in Figure 4, we find that the mean O/H of the L10 sample is much higher

($12 + \log(\text{O}/\text{H}) = 8.71$) than the value for the M12 sample ($12 + \log(\text{O}/\text{H}) = 8.57$). This difference could contribute to the discrepancy between these two local measurements of L_X/SFR .

Both the $z \sim 1.5$ and $z \sim 2.3$ stacks lie above the local L_X/SFR values, although due to the large error bars, the $z \sim 1.5$ stacks are statistically consistent with the M12 local value. The L_X/SFR of the $z \sim 2.3$ stacks are higher than, but statistically consistent with, the $z \sim 1.5$ stacks. The L_X/SFR of the $z \sim 2.3$ full sample stack is 2.3σ higher than the M12 value of $3.7 \times 10^{39} \text{ erg s}^{-1} M_\odot \text{ yr}$ and 3.1σ higher than the L10 value of $1.6 \times 10^{39} \text{ erg s}^{-1} M_\odot \text{ yr}$. Fornasini et al. (2018) find

Table 2. Stacked X-ray Properties

Stack ID	Total exposure (Ms)	Effective exposure (Ms cm ⁻²)	P_{random}	Net counts	$\langle L_X \rangle$ (10 ⁴⁰ erg s ⁻¹)	SFR Indicator	$\log \frac{\langle L_X \rangle}{(\text{SFR})_{H\alpha, \text{corr}}}$
(a)	(b)	(c)	(d)	(e)	(f)	(g)	(h)
All sSFR							
1	105.1	25779	1.5e-8	96 ± 19	19.9 ^{+3.1} _{-4.4}	H α , corr	39.94 ^{+0.06} _{-0.11}
All sSFR: redshift binning							
2	23.8	6204	3.7e-4	26 ⁺¹⁰ ₋₉	11.8 ^{+2.2} _{-4.3}	H α , corr	39.85 ^{+0.08} _{-0.19}
3	81.3	19575	3.5e-6	70 ± 17	26.8 ^{+5.6} _{-7.1}	H α , corr	39.98 ^{+0.08} _{-0.13}
All sSFR: metallicity binning							
4	50.5	12029	3.8e-4	40 ± 13	20.5 ^{+4.3} _{-6.8}	H α , corr	39.96 ^{+0.08} _{-0.18}
5	22.6	5422	2.3e-4	27 ⁺¹⁰ ₋₉	24.4 ^{+11.7} _{-4.9}	H α , corr	39.95 ^{+0.17} _{-0.10}
6	21.8	5576	3.9e-3	22 ⁺¹⁰ ₋₉	17.5 ^{+5.6} _{-7.7}	H α , corr	39.84 ^{+0.12} _{-0.25}
Restricted sSFR: metallicity binning							
7a	38.7	9245	5.8e-6	42 ± 11	27.4 ^{+7.0} _{-5.2}	H α , corr	40.12 ^{+0.10} _{-0.09}
8a	21.1	5046	4.6e-4	25 ⁺⁹ ₋₈	23.8 ^{+13.9} _{-6.2}	H α , corr	40.01 ^{+0.20} _{-0.13}
9a	16.4	4080	9.2e-3	18 ⁺⁹ ₋₈	21.4 ^{+8.8} _{-11.2}	H α , corr	39.77 ^{+0.15} _{-0.32}
7b	27.3	6868	8.2e-6	32 ⁺¹⁰ ₋₉	27.6 ^{+7.7} _{-5.6}	H α	40.03 ^{+0.11} _{-0.10}
8b	19.1	4513	1.6e-4	26 ⁺⁹ ₋₈	32.1 ^{+8.8} _{-9.5}	H α	40.04 ^{+0.11} _{-0.15}
9b	15.6	3880	1.4e-2	16 ⁺⁹ ₋₈	21.5 ^{+9.4} _{-11.9}	H α	39.78 ^{+0.16} _{-0.35}
7c	32.4	8004	5.0e-4	30 ± 10	23.1 ^{+8.0} _{-6.5}	SED	40.08 ^{+0.13} _{-0.14}
8c	21.8	5215	5.6e-4	24 ⁺⁹ ₋₈	22.0 ^{+12.2} _{-4.4}	SED	40.00 ^{+0.19} _{-0.10}
9c	17.5	4587	2.6e-2	14 ⁺⁹ ₋₈	13.1 ^{+1.5} _{-4.4}	SED	39.71 ^{+0.05} _{-0.18}
High sSFR: log(sSFR) > -8.8							
10	52.1	12656	2.4e-5	54 ± 14	25.8 ^{+5.8} _{-5.5}	H α , corr	39.84 ^{+0.09} _{-0.11}
High sSFR: redshift binning							
11	7.4	1717	8.1e-3	11 ⁺⁶ ₋₅	16.7 ^{+4.6} _{-7.6}	H α , corr	39.63 ^{+0.11} _{-0.26}
12	46.2	10939	2.9e-4	43 ± 14	29.8 ^{+8.0} _{-7.7}	H α , corr	39.91 ^{+0.10} _{-0.13}
High sSFR: metallicity binning							
13	37.3	8738	2.8e-3	30 ± 12	23.1 ^{+7.9} _{-6.2}	H α , corr	39.88 ± 0.13
14	15.6	3731	3.5e-3	19 ⁺⁹ ₋₈	26.4 ^{+6.4} _{-8.0}	H α , corr	39.71 ^{+0.09} _{-0.15}

Notes:

(c) Total exposure multiplied by *Chandra* effective area.

(e) Errors are based on Poisson statistics.

(g) Errors are based on bootstrapping.

that for X-ray stacks with $\lesssim 50$ galaxies such as these, $\langle L_X \rangle$ may be biased to higher values than the true mean by 0.15 dex;⁴ however, even accounting for this possible systematic effect, the $z \sim 2.3$ stacks have enhanced L_X/SFR compared to the L10 and M12 relations. Both the $z \sim 1.5$ and $z \sim 2.3$ full sample stacks are in good agreement with the L_X/SFR values expected from the redshift evolution of the total X-ray binary (XRB) emission measured by Lehmer et al. (2016) (shown by the dark gray long-dashed line in Figure 4; hereafter L16) and Aird et al. (2017) (shown by the dark gray short-dashed line; hereafter A17).

⁴ For small galaxy sample, $\langle L_X \rangle$ can be biased to high values due to insufficient sampling of the XRB luminosity function.

Both these previous studies also decompose the total XRB emission into an LMXB contribution proportional to M_* and an HMXB contribution proportional to SFR; the latter is traced by the light gray lines in Figure 4. The high sSFR stacks, which represent the most HMXB-dominated galaxies, are consistent (within 1.7σ) with the HMXB-only redshift evolution measured by L16 and A17. Thus, our galaxy sample supports the redshift evolution of L_X/SFR measured by other works.

6.2. The metallicity dependence of XRBs

Having established that our $z \sim 2$ galaxy sample does show enhanced L_X/SFR relative to $z = 0$ galaxies, we investigate whether this enhancement could be driven by the Z dependence of HMXBs. We tried simultaneously splitting our sample by redshift and Z but we

do not have a sufficiently high signal-to-noise ratio to obtain meaningful results. Therefore, we instead split our full sample with $1.3 < z < 2.6$ by Z , and find that splitting the sample into three bins with divisions at $12 + \log(\text{O}/\text{H}) = 8.3$ and 8.4 yields detections with $> 2.5\sigma$ significance (see stacks # 4 – 6 in Tables 1 and 2).

These three Z stacks show a slight hint of an anti-correlation between L_X/SFR and O/H . However, given the large statistical errors on L_X , the L_X/SFR values of all these bins are consistent within 1σ with a constant (Z -independent) value. Thus, from these stacks, it is not possible to determine whether the redshift evolution of L_X/SFR is driven by metallicity or some other factor since both a Z -dependent and Z -independent model can fit the data.

However, it is important to consider if systematic factors may impact this result. As mentioned in §4, a key variable which is known to affect L_X/SFR is the sSFR (Lehmer et al. 2010). Since L_{HMXB} is correlated with SFR and L_{LMXB} is correlated with M_* , galaxies with lower sSFR have higher L_X/SFR due to the larger fractional contribution of LMXBs to the X-ray emission.

The average sSFR and Z of the three stacks based our full sample are strongly anti-correlated. As reported in Table 1, the average sSFR of these three stacks spans 0.4 dex, and L_X/SFR can vary by up to 0.3 dex over this sSFR range (Lehmer et al. 2010). Such variation is comparable in magnitude to the predicted decrease of L_X/SFR with Z for the Z range probed by our stacks (Fragos et al. 2013a; Madau & Fragos 2017; hereafter F13 and M17, respectively). Thus, L_X/SFR could be inflated for the highest Z stack due to its lower sSFR and deflated for the lowest Z stack due to its higher sSFR. As a result, the fact that Z and sSFR are anti-correlated could artificially mask the expected decrease of L_X/SFR with Z .

Therefore, to reduce possible systematic effects associated with sSFR, we further restricted our sample to galaxies with $-9.3 < \log(\text{sSFR}) < -8.4$, a range of sSFR values common across all Z . This sSFR-matching criterion reduces the spread of weighted average sSFR values of the stacks to 0.15 dex (see stacks # 7a – 9a in Tables 1 and 2). This residual anti-correlation between Z and sSFR that exists in the sSFR-restricted stacks may still slightly flatten the intrinsic L_X -SFR- Z relation, but the impact on the stacked L_X/SFR should be < 0.1 dex.

The resulting L_X/SFR values versus Z are shown by the circles in Figure 5. The sSFR-restricted stacks are not consistent within 1σ uncertainties with a constant (Z -independent) L_X/SFR value. We estimate the significance of the observed anti-correlation by calculating

the probability that the data points are described by a power-law relation between L_X/SFR and Z with a negative index rather than an index ≥ 0 . The probability that the data are consistent with a negative correlation between L_X/SFR and Z is 97%. This result is robust to the statistical uncertainties in the stacked O/H values. Thus, this study provides the first direct evidence that the L_X/SFR of XRBs at $z > 0$ is anti-correlated with Z , although due to the low X-ray statistics, this conclusion is only supported with $\approx 2\sigma$ confidence.

The redshift of the sSFR-restricted stacks is roughly anti-correlated with O/H . Therefore, one might worry that the Z dependence we observe is caused by the redshift evolution of L_X/SFR , rather than vice versa. However, the weighted average redshifts of the stacks vary by < 0.2 . As found by previous studies and confirmed by our redshift-binned stacks, L_X/SFR evolves too slowly with redshift for such a small z difference to account for the 0.35 dex difference in L_X/SFR between our lowest and highest Z stacks. Therefore, the Z dependence we measure cannot be attributed to the small variation in redshift between our stacks.

The sSFR-restricted stacks are in good agreement with the best-fit theoretical models of F13 and M17, which predict an anti-correlation between L_X/SFR and Z . However, it should be noted that these models represent the X-ray emission of HMXBs alone, while our sSFR-restricted stacks likely include a significant LMXB contribution, and therefore some tension exists between our observations and these best-fit models (see §6.3 for more details).

Based on the sSFR-restricted stacks alone, we cannot determine whether the observed anti-correlation between L_X/SFR and Z at $z \sim 2$ is driven by HMXBs, LMXBs, or both. The X-ray luminosity of LMXB populations is expected to decrease with increasing Z for the same reason as for HMXBs (Fragos et al. 2013b), but the oxygen abundance of HII regions is not an adequate proxy for the metallicity of LMXBs, which are associated with the old stellar population. Furthermore, the dependence of L_{LMXB} on the age of the stellar population is predicted to be much stronger than its dependence on Z (F13; M17). Thus, L_{LMXB} is not expected to depend directly on gas-phase O/H , but if gas-phase O/H and mean stellar age are positively correlated at $z \sim 2$, then the dependence of L_{LMXB}/M_* on age may contribute to the observed anti-correlation between L_X/SFR and Z . In order for LMXBs to account for the majority of the observed trend, L_{LMXB}/M_* must be a factor of ≈ 7 higher in the lowest O/H stack compared to the highest O/H stack. According to the F13 and M17 LMXB models, such a large difference in L_{LMXB}/M_*

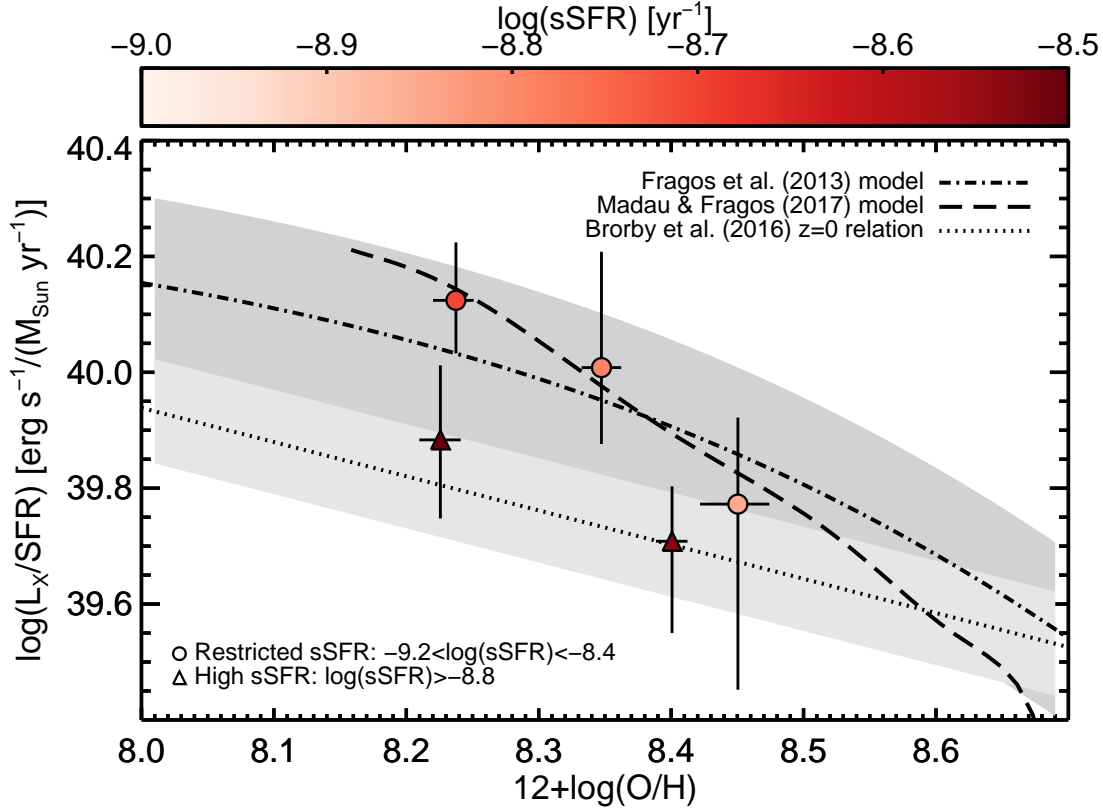


Figure 5. L_X/SFR versus oxygen abundance measurements for stacks of galaxies selected using different sSFR criteria, colored according to sSFR. The dotted line shows the local $L_X\text{-SFR-Z}$ relation from B16 based on nearby galaxies spanning $7.0 < 12+\log(\text{O}/\text{H}) < 9.0$ with corresponding error shown in light gray. The mean of the six best-fitting models from F13 is shown as a dash-dotted line, with the parameter space covered by these six models shown in dark gray. The best-fit model from M17 is shown by a dashed line, and has been converted from the Kobulnicky & Kewley (2004) R_{23} scale to the O3N2 scale from Pettini & Pagel (2004) using the conversion from Kewley & Ellison (2008). Results for a restricted sSFR range that yields a similar sSFR distribution across all Z are shown by circles; the L_X/SFR of these stacks favors a Z -dependent model. Results for high sSFR stacks are shown by triangles; this sample provides the cleanest measurement of HMXB-only L_X/SFR and is consistent with the local $L_X\text{-SFR-Z}$ relation and some theoretical models.

could be explained by a mean stellar age difference of $\gtrsim 2$ Gyr. However, the age of the Universe at $z \sim 2$ is only 3.3 Gyr. Thus, it seems probable that HMXBs are responsible for at least a significant fraction of the observed anti-correlation between L_X/SFR and Z . In §6.3, this hypothesis is tested more directly.

6.3. Comparing HMXB populations at $z = 0$ and $z \sim 2$

In order to determine whether the redshift evolution of HMXBs is driven by the Z dependence of L_X/SFR , we further need to isolate the HMXB contribution to the observed XRB Z dependence at $z \sim 2$ and test whether it is the same as that measured in the local Universe. In order to compare the normalization of the $L_X\text{-SFR-Z}$ relation for HMXBs at $z \sim 2$ and $z = 0$, it is critical to minimize the absolute LMXB contribution by focusing on high sSFR galaxies. Isolating the HMXB contribution is necessary because the local relation has been determined using only HMXB-dominated galaxies

with $\text{sSFR} > 10^{-10} \text{ yr}^{-1}$ (Brorby et al. 2016). This high sSFR selection is also important for comparing our $z \sim 2$ stacks to the F13 and M17 theoretical predictions that are based on the HMXB population alone.

As discussed in §4, while all the MOSDEF galaxies in our sample have sSFRs higher than the $\text{sSFR} > 10^{-10} \text{ yr}^{-1}$ threshold used to select HMXB-dominated galaxies in the local Universe (Lehmer et al. 2010), this transition value increases with redshift due to the evolution of L_X/SFR of HMXBs and L_X/M_* of LMXBs (Lehmer et al. 2016). Limiting our sample to $\log(\text{sSFR}) > -8.8$, which is the approximate transition value found by Lehmer et al. (2016) at $z \sim 2$, reduces the sample size by 50%, resulting in very poor signal to noise in all but the lowest of the three Z bins. Therefore, we combine galaxies in the middle Z and high Z bins to obtain a statistically meaningful second measurement. The L_X/SFR values of the two high sSFR stacks are shown as triangles in Figures 5 and 6, and the

stack properties are provided in rows # 13 – 14 of Tables 1 and 2. The L_X/SFR values of the high sSFR stacks are lower than for the full sSFR and restricted sSFR samples, suggesting that there is a non-negligible LMXB contribution to the X-ray emission in the latter samples. Based on the differences between stacks with similar Z but different $\langle s\text{SFR} \rangle$, we estimate that L_X/M_* due to LMXBs is approximately $2 - 8 \times 10^{30} \text{ erg s}^{-1} M_\odot^{-1}$. This L_X/M_* value is over an order of magnitude higher than local measurements for LMXB populations (Gilfanov 2004; Colbert et al. 2004; Lehmer et al. 2010). However, this value is consistent with the predictions of the six best-fitting population synthesis models of Fragos et al. (2013b) for $z \sim 2$ and the best model of Madau & Fragos (2017) for LMXB populations with stellar mass-weighted ages of 1.5 – 3 Gyr.

The two high sSFR stacks favor a negative correlation between L_X/SFR and Z with 86% confidence. While the significance of this result is not as high as for the restricted sSFR stacks, it suggests that the luminosity of HMXBs specifically, and not just XRBs generally, depends on Z at $z \sim 2$. The high sSFR stacks are consistent with the local L_X -SFR- Z relation and the lower L_X/SFR bound of the F13 population synthesis models. However, our high sSFR stacks exhibit significant ($> 3\sigma$) tension with the upper L_X/SFR bound of the F13 models and the best-fit M17 model. Some of this tension may be due to remaining uncertainties in the absolute calibration of SFR indicators at $z \sim 2$ and the absolute metallicity scale.

Figure 6 shows the high sSFR stacks as well as the $z \sim 2$ high sSFR stack and local L_X/SFR measurements from L10 and M12. We calculated the mean oxygen abundance of these local samples as described in §6.1; since many of the oxygen abundance estimates are based on the $M_* - z$ relation, we show the scatter of the $M_* - z$ relation from Kewley & Ellison (2008) as horizontal error bars for these local points. As shown, both the discrepancy between the local L_X/SFR measurements and the enhanced L_X/SFR of the $z \sim 2$ stack can be explained by the anti-correlation of L_X/SFR and Z . If we combine the high sSFR $z \sim 2$ stacks with at least one of the mean L_X/SFR values measured for $z = 0$, then an anti-correlation between L_X/SFR and Z is favored at $> 99.7\%$ ($> 3\sigma$) confidence. The significance of this trend established by combining mean measurements at $z \sim 2$ and $z = 0$ is comparable to the significance of the trend measured by B16 using individually detected galaxies at $z = 0$.

Thus, we find that the Z dependence of the L_X/SFR of HMXBs at $z \sim 2$ is consistent with that measured for $z = 0$ and some theoretical models. This result pro-

vides the first direct link between the observed redshift evolution of L_X/SFR and the Z dependence of HMXBs.

6.4. The impact of different SFR indicators

A key source of systematic uncertainty which may impact our results is the choice of SFR indicator. Different SFR indicators probe different star formation timescales and it is debated how different indicators evolve with redshift. As described in §2.4, for our default SFR measurements, we use $\text{H}\alpha$ SFRs with a Z -dependent $L_{\text{H}\alpha}$ -SFR conversion factor. In this section, we explore how adopting different SFR indicators would impact our results.

Figure 7 displays L_X/SFR as a function of Z based on different SFR indicators. Although we consider six different SFR indicators (see §2.3-2.4 for details), for simplicity we only show four of them in Figure 7, which provide a representative view of the impact of different SFR indicators. Since SED-derived SFRs that adopt a delayed- τ SFH are consistent within 0.1 dex with those that adopt a constant SFH, we only discuss results based on the assumption of constant SFH.

The sSFR range of the galaxies in the stacks shown in Figure 7 was restricted so that the $\langle s\text{SFR} \rangle$ of the different stacks varies by < 0.2 dex. As discussed in §6.2, we found it is important to try to match the sSFR distribution between the different Z stacks as much as possible to control for the sSFR-dependent LMXB contribution. Since the typical SFRs of the galaxies in our sample vary depending on the SFR indicator, the common sSFR range we adopt also depends on the SFR indicator. The $\log(\text{sSFR}/\text{yr}^{-1})$ ranges are -9.2 to -8.4 for the $Z = 0.02$ $\text{H}\alpha$ SFRs, -9.35 to -8.55 for the $Z = 0.004$ $\text{H}\alpha$ SFRs, -9.05 to -8.5 for the $Z = 0.02$ SED SFRs with the Calzetti et al. (2000) extinction curve, and -9.5 to -8.9 for the $Z = 0.004$ SED SFRs with the SMC extinction curve.

For each SFR indicator, we calculate the probability that the stacked L_X/SFR is anti-correlated with Z . Assuming a power-law relationship between L_X/SFR and Z , for all SFR indicators, we find that a negative power-law index is favored over an index ≥ 0 . A negative correlation is favored with 83% and 84% probability when using the $\text{H}\alpha$ -derived SFRs with $Z = 0.02$ and $Z = 0.004$, respectively, and with 99.4% and 74% confidence when using SED-derived SFRs with $Z = 0.02$ and $Z = 0.004$, respectively. Thus, while regardless of SFR indicator, an anti-correlation between the L_X/SFR of XRBs and Z at $z \sim 2$ is suggested by the data, the choice of SFR indicator does impact the significance of this result.

For each SFR indicator, we also calculate the high sSFR stacks as described in §6.3. We find that, ex-

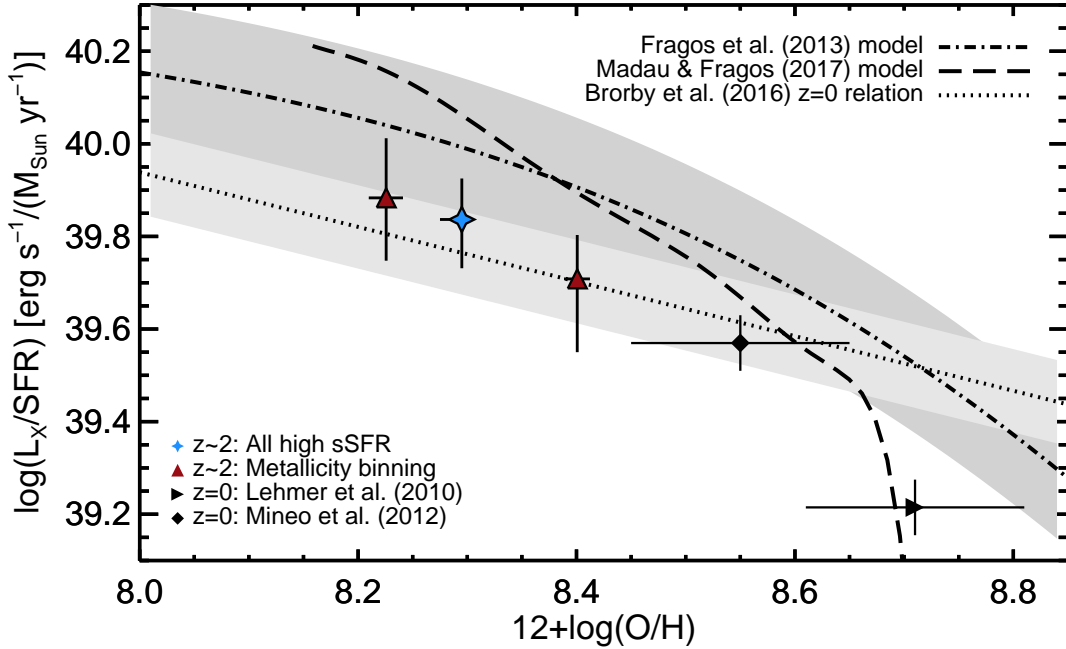


Figure 6. L_X/SFR versus stacked oxygen abundance for stacks of high sSFR ($sSFR > 10^{-8.8}$) galaxies split by O/H are shown by triangles. A stack of all sSFR galaxies at $z \sim 2$ is shown by a four-point star. These stacks provide the cleanest measurement of HMXB-only L_X/SFR . They are consistent with the local $L_X-SFR-Z$ relation and the lower theoretical predictions from F13. These stacks are inconsistent with the M17 model and the upper bound of F13 models at 3σ confidence. The diamonds show local measurements of L_X/SFR from Lehmer et al. (2010) and Mineo et al. (2012); our estimates of the mean O/H values for these samples are described in §6.1. The lines shown in this figure are as described in the caption for Figure 5.

cept for the stacks based on the SED-derived SFRs with $Z = 0.004$, all the high sSFR stacks are in good agreement with the local $L_X-SFR-Z$ relation from B16, and they are inconsistent at $> 99\%$ confidence with the M17 model and the upper L_X/SFR bound of the F13 models. In particular, these results are not affected by the $L_{H\alpha}$ -SFR conversion factor assumed. The $H\alpha$ SFRs likely provide the most reliable comparison for the local $L_X-SFR-Z$ relation, because the B16, M12, and L10 local measurements are based on UV+IR SFRs and the $H\alpha$ SFRs are in good agreement with UV+IR SFRs for the MOSDEF sample (Shivaei et al. 2016). Thus, the conclusion that the redshift evolution of L_X/SFR for high sSFR galaxies is driven by the Z dependence of HMXBs is fairly robust to the choice of SFR indicator.

6.5. Other systematic effects

We investigate other sources of systematic uncertainty and their possible impact on our results.

6.5.1. Contamination from unidentified AGN

While we have tried to screen out AGN as much as possible with multi-wavelength selection criteria, contamination from low-luminosity AGN remains a source of uncertainty. Fornasini et al. (2018) find that even

when luminous ($L_X \gtrsim 10^{42} - 10^{43}$ erg s $^{-1}$) AGN are excluded, there is evidence for obscured, low-luminosity AGN with $\langle L_X \rangle \approx 10^{41} - 10^{42}$ erg s $^{-1}$ in X-ray stacks of star-forming galaxies at $z \sim 1 - 2$. To gain some insight into how unidentified AGN may be influencing our results, we test how relaxing our AGN exclusion criteria impacts our stacks. We experimented with including identified optical, IR, or X-ray AGN as well as all identified AGN to our stacks. At most, this expands our galaxy sample by 34 galaxies and increases the $\langle L_X \rangle$ of the middle- Z and high- Z stacks by 0.1 dex (the change in $\langle L_X \rangle$ of the low- Z stack is < 0.5 dex). While the resulting L_X/SFR values of the stacks remain consistent within 1σ statistical uncertainties, the inclusion of known AGN tends to flatten the observed Z dependence. The fact that $\langle L_X \rangle$ does not significantly increase when galaxies above the Kauffmann et al. (2003) line are included in the X-ray stacks is consistent with observations that many normal star-forming galaxies at $z \sim 2$ can lie above this line due to enhanced nebular N/O or stellar α enhancement, as compared with the ionized gas and massive stars in galaxies at $z = 0$ (Masters et al. 2014; Shapley et al. 2015; Sanders et al. 2016a; Steidel et al. 2016). The comparison of L_X/SFR

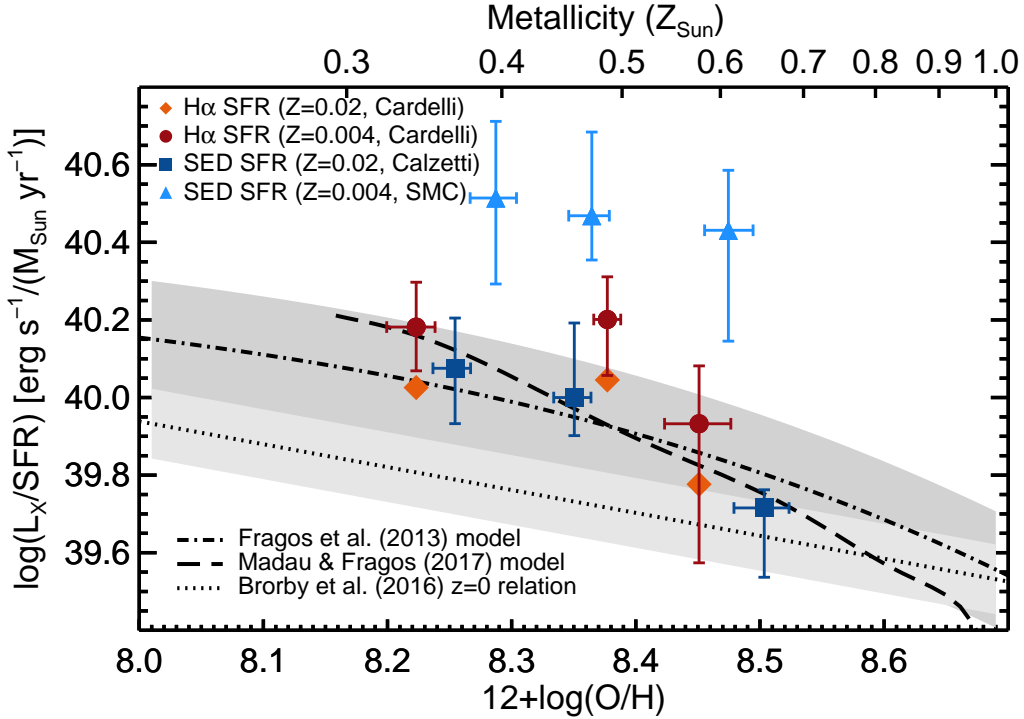


Figure 7. L_X/SFR versus stacked oxygen abundance for our galaxy sample restricted by sSFR. The top axis shows the corresponding metallicity in solar units ($Z_\odot = 0.0142$) assuming a solar abundance pattern. Orange diamonds and red circles represent results based on $H\alpha$ SFRs assuming $Z = 0.02$ and $Z = 0.004$, respectively; the 1σ error bars for these points are very similar, so only one set is shown for clarity. Dark blue squares and light blue triangles represent results based on SED SFRs, assuming $Z = 0.02$ and the Calzetti et al. (2000) attenuation curve for the former, and $Z = 0.004$ and the SMC attenuation curve for the latter. All SFR indicators favor an anti-correlation between L_X/SFR and Z , but with different significance as discussed in §6.4. The lines shown in this figure are as described in the caption for Figure 5.

of stacks with and without identified AGN suggests that contamination from unidentified, low-luminosity AGN is unlikely to significantly impact the measured L_X/SFR ; if unidentified AGN have any impact at all, this comparison implies that the true HMXB-driven relation between L_X/SFR and Z may be even steeper than that observed. Thus, the possibility of AGN contamination does not meaningfully impact our conclusions.

6.5.2. X-ray spectrum

Another source of systematic uncertainty is the X-ray spectrum. While our stacks do not have sufficient net counts for spectral fitting, hardness ratios can provide rough constraints on the spectrum. For each stack, we calculated the hardness ratio based on the net counts in the 0.5 – 2 keV (soft, S) and 2 – 7 keV (hard, H) bands using the Bayesian estimation code BEHR (Park et al. 2006), which is designed for low count statistics. The hardness ratio is defined as $(H - S)/(H + S)$. Figure 8 shows the hardness ratio of stacks #4-6 (the hardness ratios of the other stacks are very similar). As can be seen, these hardness ratios are consistent with relatively unobscured ($N_H \lesssim 10^{22} \text{ cm}^{-2}$) spectra with a photon index of $\Gamma = 1.4 - 2.5$, and our adopted spec-

tral model (unobscured, $\Gamma = 2$ power-law) falls within this range. Varying the spectral parameters within the allowed ranges results in $+/- 0.15$ dex variations in the stacked L_X , which is comparable to the statistical uncertainties; thus, the general agreement of our stacks with the F13 model and the local relation is not substantially affected by spectral variations. Changing the spectral parameters affects all stacks by the same logarithmic amount, so the relative differences between the stacks remain unchanged.

6.5.3. Redshift evolution of Z indicator and chemical abundances

Even though we use the same Z indicator as Brorby et al. (2016) to facilitate the comparison of the MOSDEF $z \sim 2$ stacks with the local $L_X\text{-SFR-}Z$ relation, it remains debated how O3N2 (and other Z indicators) may evolve with redshift. Studies of emission line ratios at $z \sim 2$ find that the N2 indicator overestimates the gas-phase O/H due to either elevated N/O or a harder stellar ionizing spectrum at fixed O/H (Masters et al. 2014; Shapley et al. 2015; Steidel et al. 2016). While these factors may also affect the O3N2 indicator, Steidel et al. (2014; 2016) present evidence that

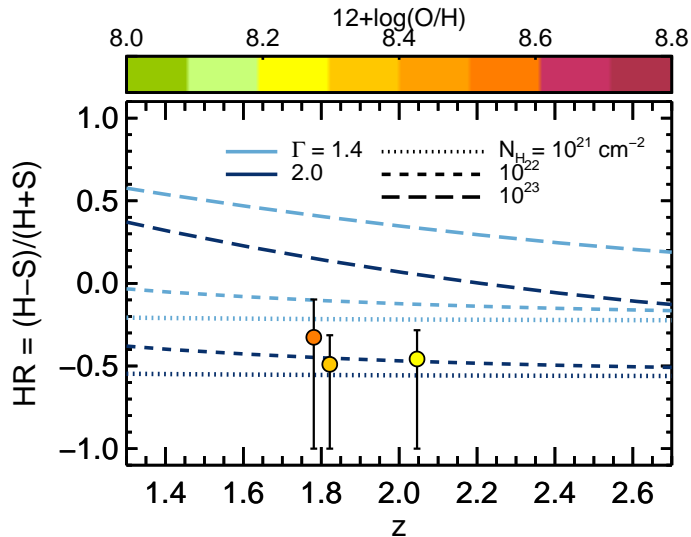


Figure 8. Hardness ratios of the three stacks based on the full sample versus weighted average redshift of the stack. Blue lines show the expected hardness ratios for sources with absorbed power-law spectra; line color represents different Γ while line style represent different column densities (N_{H}). Our stacks are consistent with relatively unobscured ($N_{\text{H}} < 10^{22} \text{ cm}^{-2}$) spectra with $\Gamma = 1.4 - 2.5$.

the O3N2 indicator is not significantly biased. While oxygen based indicators such as O_{32} or R_{23} are coming to be considered more reliable than indicators which include nitrogen (Shapley et al. 2015; Sanders et al. 2016a; Sanders et al. 2016b), adopting one of these indicators would decrease our sample size even further. Furthermore, O_{32} and R_{23} are more impacted by reddening (Sanders et al. 2018). Comparing the oxygen abundances derived using O3N2 and O_{32} for the subset of MOSDEF galaxies for which both indicators are available, we find that O/H values based on O3N2 are on average 0.13 dex lower than those derived from O_{32} . If the $\langle \text{O}/\text{H} \rangle$ values of our stacks are systematically offset by this amount, they would remain in agreement with the local $L_{\text{X}}\text{-SFR-}Z$ relation, but some of the tension with the M17 and upper F13 models would be eased.

Finally, especially when comparing our results to theoretical models, it is important to keep in mind that there may be differences between nebular O/H, which we use as a Z proxy, and stellar metallicity as defined by the F13 and M17 models. In particular, the chemical abundances in $z \sim 2$ galaxies may be different from the solar abundance pattern assumed by the models. The Z dependence of radiatively-driven stellar winds, which is the underlying cause of the Z dependence of L_{X}/SFR in HMXB population synthesis models, primarily depends on the abundance of Fe in the case of solar abundance ratios (Vink et al. 2001). However, Steidel et al. (2016)

found that $z \sim 2$ star-forming galaxies can be highly supersolar in O/Fe, as expected for a gas that is primarily enriched by core collapse supernovae. Using a small sample of $z \sim 2$ galaxies with [OIII] $\lambda 4363$ detections, including four MOSDEF galaxies, Sanders et al. (2019) similarly find that O/Fe is enhanced in the galaxies, but note that neither their sample nor the Steidel et al. (2016) sample may be representative of $z \sim 2$ galaxies.

Nonetheless, let us consider the implications if the MOSDEF $z \sim 2$ galaxies are typically supersolar in O/Fe. In this case, the line-driven winds of their stellar populations are likely dominated by C, N, and O rather than Fe. While the results of Vink et al. (2001) suggest that the Z dependence of Fe-driven and CNO-driven winds may be similar, this issue has not been investigated for $Z > 0.1Z_{\odot}$. The F13 and M17 models we use as a point of comparison, like most current models, assume solar abundance ratios for $Z \gtrsim 0.1Z_{\odot}$, and thus their appropriateness for high redshift stellar populations should be investigated.

In summary, none of these systematic effects substantially alter the conclusion that the observed redshift evolution of L_{X}/SFR is consistent with being driven by the Z dependence of HMXBs.

7. CONCLUSIONS

We have studied the X-ray emission of a sample of 79 star-forming galaxies at $1.37 < z < 2.61$ in the CANDELS fields with rest-frame optical spectra from the MOSDEF survey in order to investigate the metallicity dependence of HMXBs at $z \sim 2$. While studies of local galaxies have discovered that HMXB populations in low- Z galaxies are more luminous (e.g. Brorby et al. 2016), and the observed increase of L_{X}/SFR with redshift has been attributed to this Z dependence (Basu-Zych et al. 2013a; Lehmer et al. 2016), the connection between the redshift evolution and Z dependence of HMXBs has not been directly tested previously. In order to assess whether the Z dependence of HMXBs can account for the observed increase in L_{X}/SFR as a function of redshift, we (a) tested whether the L_{X}/SFR of HMXBs depends on Z at $z \sim 2$ and (b) compared this trend to the local $L_{\text{X}}\text{-SFR-}Z$ relation.

After removing AGN based on multi-wavelength diagnostics, we stacked the X-ray data of star-forming galaxies from the *Chandra* AEGIS-X Deep survey, the *Chandra* Deep Field North, and the *Chandra* Deep Field South. Investigating how the L_{X}/SFR of our galaxies varies when they are grouped according to redshift, Z , and sSFR, we find the following results:

1. The average L_{X}/SFR of galaxies at $z \sim 1.5$ and $z \sim 2.3$ is elevated compared to values for

local star-forming galaxies (Lehmer et al. 2010; Mineo et al. 2012). This $\approx 0.4 - 0.8$ dex enhancement is comparable to that observed for $z \sim 2$ galaxies by previous studies (Lehmer et al. 2016; Aird et al. 2017).

2. Splitting our sample into three metallicity bins, we find that L_X/SFR and Z are anti-correlated with 97% confidence at similar sSFR. This result is based on H α -derived SFRs with Z -dependent conversion factors, which we consider to be the most reliable SFR indicator available for this galaxy sample. It provides the first evidence for the metallicity dependence of XRB populations at $z > 0$. This trend is more likely to be driven by HMXBs than LMXBs, unless L_{LMXB}/M_* decreases by a factor of ≈ 7 as $12+\log(\text{O}/\text{H})$ increases from 8.25 to 8.45. Such large variation would be challenging to explain using current population synthesis models.
3. Stacking only galaxies with high sSFR ($\text{sSFR} > 1.6 \times 10^{-9} \text{ yr}^{-1}$) in order to minimize the contribution from LMXBs, we find that the L_X/SFR values of our sample are consistent with the local L_X -SFR- Z relation (Brorby et al. 2016). Thus, HMXB populations at $z \sim 2$ lie on the same L_X -SFR- Z relation as galaxies at $z = 0$. The high sSFR stacks disagree at $> 3\sigma$ confidence with the upper L_X/SFR bound of the F13 HMXB models and the best-fit HMXB population synthesis model from M17.

The three preceding results combined provide direct evidence that the enhanced L_X/SFR of $z \sim 2$ star-forming galaxies compared to high sSFR galaxies of similar M_* in the local Universe is due to the lower metallicity of the HMXB populations in high redshift galaxies. This study thus supports the hypothesis of previous works (Basu-Zych et al. 2013a; Lehmer et al. 2016) that the observed redshift evolution of L_X/SFR is the result of the Z dependence of HMXBs combined with the fact that higher-redshift galaxy samples have lower metallicities on average.

By comparing stacks with different sSFR but similar Z , we are also able to estimate that the L_X/M_* due to LMXBs is $2 - 8 \times 10^{30} \text{ erg s}^{-1} M_\odot^{-1}$ at $z \sim 2$. This estimate is an order of magnitude higher than local values (Gilfanov 2004; Lehmer et al. 2010, but consistent with predictions from the F13 and M17 LMXB population synthesis models.

Possible AGN contamination, the assumed X-ray spectrum, and systematics associated with the metallicity measurements do not significantly impact our con-

clusions. The choice of SFR indicator can substantially affect the absolute L_X/SFR values, but the result that L_X/SFR varies with Z and that this trend is consistent with the L_X -SFR- Z local relation are fairly robust to the choice of SFR indicator. As our understanding of SFR indicators at high redshift improves, it will be important to revisit these issues.

Furthermore, since there is evidence that the stellar populations at $z \sim 2$ may have supersolar O/Fe, it is also important to investigate the effect of α -element enhanced abundances on HMXB population synthesis models. Current models assume solar abundance ratios, and have not studied the impact of CNO rather than Fe driven stellar winds on HMXB populations with $Z > 0.1Z_\odot$.

While our study only probes the metallicity range of $12+\log(\text{O}/\text{H}) = 8.0 - 8.8$, our results indicate that the B16 relation and the F13 models with lower L_X/SFR normalizations provide reasonable estimates of the X-ray emission of HMXBs out to high-redshift. Thus, we encourage the adoption of these scaling relations by studies searching for faint X-ray AGN or investigating the effect of X-ray heating on the epoch of reionization.

While this study provides the first direct connection between the redshift evolution and Z dependence of HMXBs, future work is required to improve the statistical significance of this result and to constrain theoretical models of the Z dependence of HMXBs. Larger samples of galaxies with Z measurements are crucial to reduce the statistical uncertainties of the stacked L_X . Future thirty-meter class telescopes will be critical for increasing such measurements at high redshifts. Expanding this study to other redshift ranges will also further test whether the observed redshift evolution is driven by the HMXB Z dependence as found by this study. Furthermore, improving measurements of the local L_X -SFR- Z relation by increasing the local galaxy sample size and determining its dependence on additional variables such as sSFR is important as it provides a benchmark for high-redshift studies.

With current X-ray instruments, the scatter in the L_X -SFR- Z relation can only be studied using nearby galaxy samples, while higher-redshift studies depend on stacking or other statistical techniques. In the future, the *Athena X-ray Observatory* will enable the detection of large samples of individual XRB-dominated galaxies out to $z \sim 1$, and the *Lynx X-ray Observatory* would push these detection limits out to $z \sim 6$. Combined with accurate Z and SFR measurements from *JWST*, the large samples of individually detected XRB-dominated galaxies provided by these future X-ray missions will enable much more detailed investigations of the multivariate

dependence of L_{XRB} and its scatter on galaxy properties and redshift. These future analyses will help provide stronger constraints on models of stellar evolution, the progenitor channels of gravitational wave sources, and the X-ray heating of the intergalactic medium in the early Universe.

We thank G. Fabbiano and M. Elvis for fruitful conversations about this study. FMF and MK acknowledge support from *Chandra* grant 17620679. We acknowledge support from NSF AAG grants AST1312780, 1312547, 1312764, and 1313171, archival grant AR13907 provided by NASA through the Space Telescope Science Institute, and grant NNX16AF54G from the NASA ADAP program. We additionally acknowledge the 3D-HST collaboration for providing spectroscopic and photometric catalogs used in the MOSDEF survey. The scientific results reported in this paper are based on observations made by the *Chandra X-ray Observatory*. This study

also made use of data obtained at the W.M. Keck Observatory, which is operated as a scientific partnership among the California Institute of Technology, the University of California, and the National Aeronautics and Space Administration. The Observatory was made possible by the generous financial support of the W.M. Keck Foundation. We wish to extend special thanks to those of Hawaiian ancestry, on whose sacred mountain we are privileged to be guests. Without their generous hospitality, this work would not have been possible. This study is also based on observations made with the NASA/ESA Hubble Space Telescope, which is operated by the Association of Universities for Research in Astronomy, Inc., under NASA contract NAS 5-26555.

Software: CIAO (Fruscione et al. 2006), BEHR (Park et al. 2006)

Facilities: Chandra X-ray Observatory, Keck Observatory

REFERENCES

- Abbott, B. P., Abbott, R., Abbott, T. D., et al. 2016, ApJL, 818, L22, doi: [10.3847/2041-8205/818/2/L22](https://doi.org/10.3847/2041-8205/818/2/L22)
- Aird, J., Coil, A. L., & Georgakakis, A. 2017, MNRAS, 465, 3390, doi: [10.1093/mnras/stw2932](https://doi.org/10.1093/mnras/stw2932)
- Aird, J., Coil, A. L., Georgakakis, A., et al. 2015, MNRAS, 451, 1892, doi: [10.1093/mnras/stv1062](https://doi.org/10.1093/mnras/stv1062)
- Ajello, M., Greiner, J., Sato, G., et al. 2008, ApJ, 689, 666, doi: [10.1086/592595](https://doi.org/10.1086/592595)
- Alexander, D. M., Bauer, F. E., Brandt, W. N., et al. 2003, AJ, 126, 539, doi: [10.1086/376473](https://doi.org/10.1086/376473)
- Antoniou, V., & Zezas, A. 2016, MNRAS, 459, 528, doi: [10.1093/mnras/stw167](https://doi.org/10.1093/mnras/stw167)
- Asplund, M., Grevesse, N., Sauval, A. J., & Scott, P. 2009, ARA&A, 47, 481, doi: [10.1146/annurev.astro.46.060407.145222](https://doi.org/10.1146/annurev.astro.46.060407.145222)
- Azadi, M., Coil, A. L., Aird, J., et al. 2017, ApJ, 835, 27, doi: [10.3847/1538-4357/835/1/27](https://doi.org/10.3847/1538-4357/835/1/27)
- Baldwin, J. A., Phillips, M. M., & Terlevich, R. 1981, PASP, 93, 5, doi: [10.1086/130766](https://doi.org/10.1086/130766)
- Basu-Zych, A. R., Lehmer, B. D., Hornschemeier, A. E., et al. 2013a, ApJ, 762, 45, doi: [10.1088/0004-637X/762/1/45](https://doi.org/10.1088/0004-637X/762/1/45)
- . 2013b, ApJ, 774, 152, doi: [10.1088/0004-637X/774/2/152](https://doi.org/10.1088/0004-637X/774/2/152)
- Belczynski, K., Holz, D. E., Bulik, T., & O’Shaughnessy, R. 2016, Nature, 534, 512, doi: [10.1038/nature18322](https://doi.org/10.1038/nature18322)
- Belczynski, K., Kalogera, V., Zezas, A., & Fabbiano, G. 2004, ApJL, 601, L147, doi: [10.1086/382131](https://doi.org/10.1086/382131)
- Bodaghee, A., Tomsick, J. A., Rodriguez, J., & James, J. B. 2012, ApJ, 744, 108, doi: [10.1088/0004-637X/744/2/108](https://doi.org/10.1088/0004-637X/744/2/108)
- Brorby, M., Kaaret, P., & Prestwich, A. 2014, MNRAS, 441, 2346, doi: [10.1093/mnras/stu736](https://doi.org/10.1093/mnras/stu736)
- Brorby, M., Kaaret, P., Prestwich, A., & Mirabel, I. F. 2016, MNRAS, 457, 4081, doi: [10.1093/mnras/stw284](https://doi.org/10.1093/mnras/stw284)
- Bruzual, G., & Charlot, S. 2003, MNRAS, 344, 1000, doi: [10.1046/j.1365-8711.2003.06897.x](https://doi.org/10.1046/j.1365-8711.2003.06897.x)
- Calzetti, D., Armus, L., Bohlin, R. C., et al. 2000, ApJ, 533, 682, doi: [10.1086/308692](https://doi.org/10.1086/308692)
- Capak, P., Cowie, L. L., Hu, E. M., et al. 2004, AJ, 127, 180, doi: [10.1086/380611](https://doi.org/10.1086/380611)
- Cappelluti, N., Li, Y., Ricarte, A., et al. 2017, ApJ, 837, 19, doi: [10.3847/1538-4357/aa5ea4](https://doi.org/10.3847/1538-4357/aa5ea4)
- Cardelli, J. A., Clayton, G. C., & Mathis, J. S. 1989, ApJ, 345, 245, doi: [10.1086/167900](https://doi.org/10.1086/167900)
- Chabrier, G. 2003, PASP, 115, 763, doi: [10.1086/376392](https://doi.org/10.1086/376392)
- Civano, F., Marchesi, S., Comastri, A., et al. 2016, ApJ, 819, 62, doi: [10.3847/0004-637X/819/1/62](https://doi.org/10.3847/0004-637X/819/1/62)
- Coil, A. L., Aird, J., Reddy, N., et al. 2015, ApJ, 801, 35, doi: [10.1088/0004-637X/801/1/35](https://doi.org/10.1088/0004-637X/801/1/35)
- Colbert, E. J. M., Heckman, T. M., Ptak, A. F., Strickland, D. K., & Weaver, K. A. 2004, ApJ, 602, 231, doi: [10.1086/380899](https://doi.org/10.1086/380899)
- Conroy, C., Gunn, J. E., & White, M. 2009, ApJ, 699, 486, doi: [10.1088/0004-637X/699/1/486](https://doi.org/10.1088/0004-637X/699/1/486)
- Cowie, L. L., Barger, A. J., & Hasinger, G. 2012, ApJ, 748, 50, doi: [10.1088/0004-637X/748/1/50](https://doi.org/10.1088/0004-637X/748/1/50)

- Davis, M., Guhathakurta, P., Konidaris, N. P., et al. 2007, *ApJL*, 660, L1, doi: [10.1086/517931](https://doi.org/10.1086/517931)
- Donley, J. L., Koekemoer, A. M., Brusa, M., et al. 2012, *ApJ*, 748, 142, doi: [10.1088/0004-637X/748/2/142](https://doi.org/10.1088/0004-637X/748/2/142)
- Douna, V. M., Pellizza, L. J., Mirabel, I. F., & Pedrosa, S. E. 2015, *A&A*, 579, A44, doi: [10.1051/0004-6361/201525617](https://doi.org/10.1051/0004-6361/201525617)
- Dray, L. M. 2006, *MNRAS*, 370, 2079, doi: [10.1111/j.1365-2966.2006.10635.x](https://doi.org/10.1111/j.1365-2966.2006.10635.x)
- Fazio, G. G., Hora, J. L., Allen, L. E., et al. 2004, *ApJS*, 154, 10, doi: [10.1086/422843](https://doi.org/10.1086/422843)
- Fornasini, F. M., Civano, F., Fabbiano, G., et al. 2018, *ApJ*, 865, 43, doi: [10.3847/1538-4357/aada4e](https://doi.org/10.3847/1538-4357/aada4e)
- Fragos, T., Lehmer, B. D., Naoz, S., Zezas, A., & Basu-Zych, A. 2013a, *ApJL*, 776, L31, doi: [10.1088/2041-8205/776/2/L31](https://doi.org/10.1088/2041-8205/776/2/L31)
- Fragos, T., Lehmer, B., Tremmel, M., et al. 2013b, *ApJ*, 764, 41, doi: [10.1088/0004-637X/764/1/41](https://doi.org/10.1088/0004-637X/764/1/41)
- Freeman, W. R., Siana, B., Kriek, M., et al. 2019, *ApJ*, 873, 102, doi: [10.3847/1538-4357/ab0655](https://doi.org/10.3847/1538-4357/ab0655)
- Fruscione, A., McDowell, J. C., Allen, G. E., et al. 2006, in *Society of Photo-Optical Instrumentation Engineers (SPIE) Conference Series*, Vol. 6270, *Proc. SPIE*, 62701V
- Gialalisco, M., Ferguson, H. C., Koekemoer, A. M., et al. 2004, *ApJL*, 600, L93, doi: [10.1086/379232](https://doi.org/10.1086/379232)
- Gilfanov, M. 2004, *MNRAS*, 349, 146, doi: [10.1111/j.1365-2966.2004.07473.x](https://doi.org/10.1111/j.1365-2966.2004.07473.x)
- Gilfanov, M., Grimm, H.-J., & Sunyaev, R. 2004, *MNRAS*, 347, L57, doi: [10.1111/j.1365-2966.2004.07450.x](https://doi.org/10.1111/j.1365-2966.2004.07450.x)
- Gordon, K. D., Clayton, G. C., Misselt, K. A., Landolt, A. U., & Wolff, M. J. 2003, *ApJ*, 594, 279, doi: [10.1086/376774](https://doi.org/10.1086/376774)
- Grimm, H.-J., Gilfanov, M., & Sunyaev, R. 2003, *MNRAS*, 339, 793, doi: [10.1046/j.1365-8711.2003.06224.x](https://doi.org/10.1046/j.1365-8711.2003.06224.x)
- Grogin, N. A., Kocevski, D. D., Faber, S. M., et al. 2011, *ApJS*, 197, 35, doi: [10.1088/0067-0049/197/2/35](https://doi.org/10.1088/0067-0049/197/2/35)
- Gruber, D. E., Matteson, J. L., Peterson, L. E., & Jung, G. V. 1999, *ApJ*, 520, 124, doi: [10.1086/307450](https://doi.org/10.1086/307450)
- Gwyn, S. D. J. 2012, *AJ*, 143, 38, doi: [10.1088/0004-6256/143/2/38](https://doi.org/10.1088/0004-6256/143/2/38)
- Hao, C.-N., Kennicutt, R. C., Johnson, B. D., et al. 2011, *ApJ*, 741, 124, doi: [10.1088/0004-637X/741/2/124](https://doi.org/10.1088/0004-637X/741/2/124)
- Horne, K. 1986, *PASP*, 98, 609, doi: [10.1086/131801](https://doi.org/10.1086/131801)
- Hsieh, B.-C., Wang, W.-H., Hsieh, C.-C., et al. 2012, *ApJS*, 203, 23, doi: [10.1088/0067-0049/203/2/23](https://doi.org/10.1088/0067-0049/203/2/23)
- Iben, Jr., I., Tutukov, A. V., & Yungelson, L. R. 1995, *ApJS*, 100, 217, doi: [10.1086/192217](https://doi.org/10.1086/192217)
- Kaaret, P. 2014, *MNRAS*, 440, L26, doi: [10.1093/mnras/slu018](https://doi.org/10.1093/mnras/slu018)
- Kaaret, P., Schmitt, J., & Gorski, M. 2011, *ApJ*, 741, 10, doi: [10.1088/0004-637X/741/1/10](https://doi.org/10.1088/0004-637X/741/1/10)
- Kauffmann, G., Heckman, T. M., Tremonti, C., et al. 2003, *MNRAS*, 346, 1055, doi: [10.1111/j.1365-2966.2003.07154.x](https://doi.org/10.1111/j.1365-2966.2003.07154.x)
- Kewley, L. J., & Ellison, S. L. 2008, *ApJ*, 681, 1183, doi: [10.1086/587500](https://doi.org/10.1086/587500)
- Kobulnicky, H. A., & Kewley, L. J. 2004, *ApJ*, 617, 240, doi: [10.1086/425299](https://doi.org/10.1086/425299)
- Koekemoer, A. M., Faber, S. M., Ferguson, H. C., et al. 2011, *ApJS*, 197, 36, doi: [10.1088/0067-0049/197/2/36](https://doi.org/10.1088/0067-0049/197/2/36)
- Kriek, M., van Dokkum, P. G., Labbé, I., et al. 2009, *ApJ*, 700, 221, doi: [10.1088/0004-637X/700/1/221](https://doi.org/10.1088/0004-637X/700/1/221)
- Kriek, M., Shapley, A. E., Reddy, N. A., et al. 2015, *ApJS*, 218, 15, doi: [10.1088/0067-0049/218/2/15](https://doi.org/10.1088/0067-0049/218/2/15)
- Laigle, C., McCracken, H. J., Ilbert, O., et al. 2016, *ApJS*, 224, 24, doi: [10.3847/0067-0049/224/2/24](https://doi.org/10.3847/0067-0049/224/2/24)
- Laird, E. S., Nandra, K., Georgakakis, A., et al. 2009, *ApJS*, 180, 102, doi: [10.1088/0067-0049/180/1/102](https://doi.org/10.1088/0067-0049/180/1/102)
- Lawrence, A., Warren, S. J., Almaini, O., et al. 2007, *MNRAS*, 379, 1599, doi: [10.1111/j.1365-2966.2007.12040.x](https://doi.org/10.1111/j.1365-2966.2007.12040.x)
- Lehmer, B. D., Alexander, D. M., Bauer, F. E., et al. 2010, *ApJ*, 724, 559, doi: [10.1088/0004-637X/724/1/559](https://doi.org/10.1088/0004-637X/724/1/559)
- Lehmer, B. D., Basu-Zych, A. R., Mineo, S., et al. 2016, *ApJ*, 825, 7, doi: [10.3847/0004-637X/825/1/7](https://doi.org/10.3847/0004-637X/825/1/7)
- Leung, G. C. K., Coil, A. L., Azadi, M., et al. 2017, *ApJ*, 849, 48, doi: [10.3847/1538-4357/aa9024](https://doi.org/10.3847/1538-4357/aa9024)
- Linden, T., Kalogera, V., Sepinsky, J. F., et al. 2010, *ApJ*, 725, 1984, doi: [10.1088/0004-637X/725/2/1984](https://doi.org/10.1088/0004-637X/725/2/1984)
- Luo, B., Brandt, W. N., Xue, Y. Q., et al. 2017, *ApJS*, 228, 2, doi: [10.3847/1538-4365/228/1/2](https://doi.org/10.3847/1538-4365/228/1/2)
- Madau, P., & Fragos, T. 2017, *ApJ*, 840, 39, doi: [10.3847/1538-4357/aa6af9](https://doi.org/10.3847/1538-4357/aa6af9)
- Mapelli, M., Ripamonti, E., Zampieri, L., & Colpi, M. 2011, *Astronomische Nachrichten*, 332, 414, doi: [10.1002/asna.201011511](https://doi.org/10.1002/asna.201011511)
- Masters, D., McCarthy, P., Siana, B., et al. 2014, *ApJ*, 785, 153, doi: [10.1088/0004-637X/785/2/153](https://doi.org/10.1088/0004-637X/785/2/153)
- McLean, I. S., Steidel, C. C., Epps, H. W., et al. 2012, in *Proc. SPIE*, Vol. 8446, *Ground-based and Airborne Instrumentation for Astronomy IV*, 84460J
- Mezcua, M. 2017, *International Journal of Modern Physics D*, 26, 1730021, doi: [10.1142/S021827181730021X](https://doi.org/10.1142/S021827181730021X)
- Mezcua, M., Civano, F., Fabbiano, G., Miyaji, T., & Marchesi, S. 2016, *ApJ*, 817, 20, doi: [10.3847/0004-637X/817/1/20](https://doi.org/10.3847/0004-637X/817/1/20)
- Mineo, S., Gilfanov, M., & Sunyaev, R. 2012, *MNRAS*, 419, 2095, doi: [10.1111/j.1365-2966.2011.19862.x](https://doi.org/10.1111/j.1365-2966.2011.19862.x)

- Mirabel, I. F., Dijkstra, M., Laurent, P., Loeb, A., & Pritchard, J. R. 2011, *A&A*, 528, A149, doi: [10.1051/0004-6361/201016357](https://doi.org/10.1051/0004-6361/201016357)
- Momcheva, I. G., Brammer, G. B., van Dokkum, P. G., et al. 2016, *ApJS*, 225, 27, doi: [10.3847/0067-0049/225/2/27](https://doi.org/10.3847/0067-0049/225/2/27)
- Nandra, K., Laird, E. S., Aird, J. A., et al. 2015, *ApJS*, 220, 10, doi: [10.1088/0067-0049/220/1/10](https://doi.org/10.1088/0067-0049/220/1/10)
- Park, T., Kashyap, V. L., Siemiginowska, A., et al. 2006, *ApJ*, 652, 610, doi: [10.1086/507406](https://doi.org/10.1086/507406)
- Parsons, A. R., Liu, A., Aguirre, J. E., et al. 2014, *ApJ*, 788, 106, doi: [10.1088/0004-637X/788/2/106](https://doi.org/10.1088/0004-637X/788/2/106)
- Persic, M., Rephaeli, Y., Braito, V., et al. 2004, *A&A*, 419, 849, doi: [10.1051/0004-6361:20034500](https://doi.org/10.1051/0004-6361:20034500)
- Pettini, M., & Pagel, B. E. J. 2004, *MNRAS*, 348, L59, doi: [10.1111/j.1365-2966.2004.07591.x](https://doi.org/10.1111/j.1365-2966.2004.07591.x)
- Prestwich, A. H., Tsantaki, M., Zezas, A., et al. 2013, *ApJ*, 769, 92, doi: [10.1088/0004-637X/769/2/92](https://doi.org/10.1088/0004-637X/769/2/92)
- Ranalli, P., Comastri, A., & Setti, G. 2003, *A&A*, 399, 39, doi: [10.1051/0004-6361:20021600](https://doi.org/10.1051/0004-6361:20021600)
- Rangel, C., Nandra, K., Laird, E. S., & Orange, P. 2013, *MNRAS*, 428, 3089, doi: [10.1093/mnras/sts256](https://doi.org/10.1093/mnras/sts256)
- Reddy, N. A., Pettini, M., Steidel, C. C., et al. 2012, *ApJ*, 754, 25, doi: [10.1088/0004-637X/754/1/25](https://doi.org/10.1088/0004-637X/754/1/25)
- Reddy, N. A., Kriek, M., Shapley, A. E., et al. 2015, *ApJ*, 806, 259, doi: [10.1088/0004-637X/806/2/259](https://doi.org/10.1088/0004-637X/806/2/259)
- Reddy, N. A., Shapley, A. E., Sanders, R. L., et al. 2018, arXiv e-prints. <https://arxiv.org/abs/1811.11767>
- Rodriguez, C. L., Zevin, M., Pankow, C., Kalogera, V., & Rasio, F. A. 2016, *ApJL*, 832, L2, doi: [10.3847/2041-8205/832/1/L2](https://doi.org/10.3847/2041-8205/832/1/L2)
- Sanders, R. L., Shapley, A. E., Kriek, M., et al. 2015, *ApJ*, 799, 138, doi: [10.1088/0004-637X/799/2/138](https://doi.org/10.1088/0004-637X/799/2/138)
- . 2016a, *ApJ*, 816, 23, doi: [10.3847/0004-637X/816/1/23](https://doi.org/10.3847/0004-637X/816/1/23)
- . 2016b, *ApJ*, 825, L23, doi: [10.3847/2041-8205/825/2/L23](https://doi.org/10.3847/2041-8205/825/2/L23)
- . 2018, *ApJ*, 858, 99, doi: [10.3847/1538-4357/aabcbdb](https://doi.org/10.3847/1538-4357/aabcbdb)
- Sanders, R. L., Shapley, A. E., Reddy, N. A., et al. 2019, arXiv e-prints, arXiv:1907.00013. <https://arxiv.org/abs/1907.00013>
- Scoville, N., Aussel, H., Brusa, M., et al. 2007, *ApJS*, 172, 1, doi: [10.1086/516585](https://doi.org/10.1086/516585)
- Shapley, A. E., Reddy, N. A., Kriek, M., et al. 2015, *ApJ*, 801, 88, doi: [10.1088/0004-637X/801/2/88](https://doi.org/10.1088/0004-637X/801/2/88)
- Shivaei, I., Reddy, N. A., Shapley, A. E., et al. 2015, *ApJ*, 815, 98, doi: [10.1088/0004-637X/815/2/98](https://doi.org/10.1088/0004-637X/815/2/98)
- Shivaei, I., Kriek, M., Reddy, N. A., et al. 2016, *ApJL*, 820, L23, doi: [10.3847/2041-8205/820/2/L23](https://doi.org/10.3847/2041-8205/820/2/L23)
- Skelton, R. E., Whitaker, K. E., Momcheva, I. G., et al. 2014, *ApJS*, 214, 24, doi: [10.1088/0067-0049/214/2/24](https://doi.org/10.1088/0067-0049/214/2/24)
- Steidel, C. C., Strom, A. L., Pettini, M., et al. 2016, *ApJ*, 826, 159, doi: [10.3847/0004-637X/826/2/159](https://doi.org/10.3847/0004-637X/826/2/159)
- Steidel, C. C., Rudie, G. C., Strom, A. L., et al. 2014, *ApJ*, 795, 165, doi: [10.1088/0004-637X/795/2/165](https://doi.org/10.1088/0004-637X/795/2/165)
- Strom, A. L., Steidel, C. C., Rudie, G. C., et al. 2017, *ApJ*, 836, 164, doi: [10.3847/1538-4357/836/2/164](https://doi.org/10.3847/1538-4357/836/2/164)
- Veilleux, S., & Osterbrock, D. E. 1987, *ApJS*, 63, 295, doi: [10.1086/191166](https://doi.org/10.1086/191166)
- Vink, J. S., de Koter, A., & Lamers, H. J. G. L. M. 2001, *A&A*, 369, 574, doi: [10.1051/0004-6361:20010127](https://doi.org/10.1051/0004-6361:20010127)